The Nucleation-Annihilation Dynamics of Hotspot Patterns for a Reaction-Diffusion System of Urban Crime with Police Deployment

Chunyi Gai and Michael J. Ward

Department of Mathematics
University of British Columbia, Vancouver, Canada

March 15, 2024

Abstract

A hybrid asymptotic-numerical approach is developed to study the existence and linear stability of steady-state hotspot patterns for a three-component 1-D reaction-diffusion (RD) system that models urban crime with police intervention. Our analysis is focused on a new scaling regime in the RD system where there are two distinct competing mechanisms of hotspot annihilation and creation that, when coincident in a parameter space, lead to complex spatio-temporal dynamics of hotspot patterns. Hotspot annihilation events are shown numerically to be triggered by an asynchronous oscillatory instability of the hotspot amplitudes that arises from a secondary instability on the branch of periodic solutions that emerges from a Hopf bifurcation of the steady-state solution. In addition, hotspots can be nucleated from a quiescent background when the criminal diffusivity is below a saddle-node bifurcation threshold of hotspot equilibria, which we estimate from our asymptotic analysis. To investigate instabilities of hotspot steady-states, the spectrum of the linearization around a two-boundary hotspot pattern is computed, and instability thresholds due to either zero-eigenvalue crossings or Hopf bifurcations are shown. The bifurcation software *pde2path* is used to follow the branch of periodic solutions and detect the onset of the secondary instability. Overall, these results provide a phase diagram in parameter space where distinct types of dynamical behaviors occur. In one region of this phase diagram, where the police diffusivity is small, a two-boundary hotspot steady-state is unstable to an asynchronous oscillatory instability in the hotspot amplitudes. This instability typically triggers a nonlinear process leading to the annihilation of one of the hotspots. However, for parameter values where this instability is coincident with the non-existence of a one-hotspot steady-state, we show that hotspot patterns undergo complex "nucleation-annihilation" dynamics that are characterized by large-scale persistent oscillations of the hotspot amplitudes. In this way, our results identify parameter ranges in the three-component crime model where the effect of police intervention is to simply displace crime between adjacent hotspots and where new crime hotspots regularly emerge "spontaneously" from regions that were previously free of crime. More generally, it is suggested that when these annihilation and nucleation mechanisms are coincident for other multi-hotspot patterns, the problem of predicting the spatial-temporal distribution of crime is largely intractable.

1 Introduction

Crimes due to residential burglaries are not generally uniformly distributed within cities. Instead, they are denser in some areas and sparser in others, which results in crime patterns that tend to be spatially localized in certain hotspots of criminal activity [3] (see also [31]). The development of agent-based and PDE continuum-based mathematical modeling approaches to predict spatial patterns of urban crime originates from the foundational

1

studies in [25, 24, 23] that are based on postulated interactions between two primary field variables: the attractiveness of the site for burglary and the density of criminals. A key ingredient in their modeling framework is that crime hotspots can result from a "near-repeat" victimization effect, which suggests that a crime at one site can create an environment that encourages further crime events near that site within a certain time period [3].

To model the effect of police intervention on crime hotspots two distinct approaches have been used. By using agent-based simulation modeling, various detailed real-world policing strategies can and have been incorporated (cf. [10], [5]). A second direction, more amenable to analysis, is to formulate and analyze three-component PDE-based RD systems that include the police density as an extra field variable (cf. [10], [17], [32], [21], [27], [4]). For an extended three-component system, an optimal control strategy for the policing effort, which tracks a dynamically evolving crime pattern, was developed in [32] to minimize the overall crime rate.

One primary goal of this article, as discussed below, is to analyze two competing mechanisms that are responsible for producing complex spatio-temporal hotspot patterns for a three-component 1-D RD model of urban crime with police deployment. On the interval $|x| < L$, this RD system is given in dimensionless form by

$$A_t = \varepsilon^2 A_{xx} - A + \rho A + \alpha \,, \tag{1.1a}$$

$$\rho_t = D(\rho_x - 2\rho A_x/A)_x - \rho A + \gamma - \alpha - \rho U \,, \tag{1.1b}$$

$$\tau U_t = D(U_x - qUA_x/A)_x \,, \tag{1.1c}$$

where $A_x(\pm L) = \rho_x(\pm L) = U_x(\pm L) = 0$. Here $A(x,t)$ is the attractiveness of the environment to burglary, while $\rho(x,t)$ and $U(x,t)$ are the population densities of criminals and police, respectively. The constant $\alpha > 0$ is the spatially uniform baseline attractiveness, $\gamma - \alpha$ represents the constant rate at which new criminals are introduced, D is the criminal diffusivity, and $D_p \equiv D/\tau$ is the police diffusivity. The chemotactic drift term $-2D(\rho A_x/A)_x$ represents the tendency of criminals to move towards sites with higher attractiveness. Likewise, the police are assumed to undergo a biased random walk toward areas of higher attractiveness, with the parameter $q > 1$ measuring the degree of focus in the police patrol towards the maxima of the attractiveness field A. In particular, the choice $q = 2$ is the "cops-on-the-dots" strategy (cf. [10, 32]) where the police have the same drift tendency as the criminals towards maxima of A. Moreover, we will assume, as in [13] and [26], that

$$\gamma > 3\alpha/2 \,. \tag{1.2}$$

On this range of γ, the uniform steady-state solution to (1.1) in the absence of police, given by $A_e = \gamma$ and $\rho_e = 1 - \alpha/\gamma$, is unstable as $\varepsilon \to 0$ to the formation of hotspots [26]. By integrating (1.1c) over the domain, we conclude that the total "mass" of police is conserved in time, and we define U_0 by

$$U_0 \equiv \int_{-L}^{L} U(x,t) \, dx \,. \tag{1.3}$$

To analyze (1.1) it is convenient to introduce the new variables V and u, as introduced in [13, 26, 4], defined by

$$\rho = VA^2 \,, \qquad U = uA^q \,. \tag{1.4}$$

In terms of these variables, (1.1) transforms on $-L < x < L$ to

$$A_t = \varepsilon^2 A_{xx} - A + VA^3 + \alpha \,, \tag{1.5a}$$

$$(VA^2)_t = D(A^2 V_x)_x - VA^3 + \gamma - \alpha - uVA^{2+q} \,, \tag{1.5b}$$

$$\tau(uA^q)_t = D(A^q u_x)_x \,. \tag{1.5c}$$

Our analysis of (1.1) and (1.5) will focus on the singularly perturbed limit $\varepsilon \ll 1$, where the attractiveness field can be localized within certain hotspot regions. A numerically-computed two-hotspot steady-state pattern
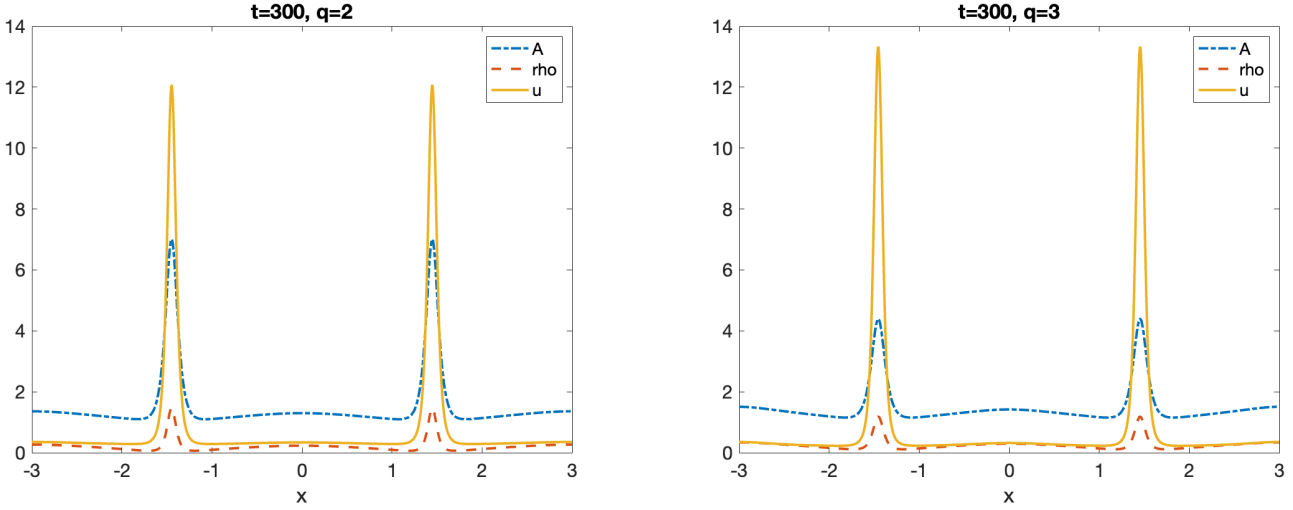
2

Figure 1: Two-hotspot steady states of (1.1), with $q = 2$ (left) and $q = 3$ (right), computed from *FlexPDE* [6] for an initial condition that is a random perturbation of the spatially uniform steady-state. Parameters: $\alpha = 1$, $\gamma = 2$, $\varepsilon = 0.05$, $L = 3$, $D = 4$ and $U_0 = 5$.

from the time-dependent problem (1.1) is illustrated in Figure 1 on the domain $[-3, 3]$ for $q = 2$ and $q = 3$, with the other parameters as in the figure caption. For $q = 3$ we observe from this figure that the spatial extent of U is more focused as compared to the "cops-on-the-dots" case $q = 2$.

When $U_0 = 0$, (1.1) reduces to a two-component PDE system, which was first derived and analyzed in [25, 24]. This reduced system has been studied extensively. A rigorous existence theory was established in [20, 19, 22]. The computation of global snaking-type bifurcation diagrams was undertaken in [14] for the regime where $\alpha < \gamma < 3\alpha/2$. Hotspot equilibria for the regime $D \gg 1$ were constructed formally in [13] using matched asymptotic expansions and established rigorously in [1] by using a Lyapunov-Schmidt reduction. A weakly nonlinear analysis was implemented in [8] to analyze the emergence of spatial patterns near the Turing bifurcation point associated with the spatially uniform steady-state. The nucleation behavior of hotspot patterns and their slow dynamics in the regime $D = \mathcal{O}(1)$ was analyzed in [26] in the singular limit $\varepsilon \ll 1$.

In contrast, there are relatively few studies for the analysis of spatio-temporal pattern formation for the three-component crime model with police. For the regime $D = \mathcal{O}(\varepsilon^{-2}) \gg 1$, the existence and linear stability of hotspot steady-states for the simple police interaction model, in which $-\rho U$ in (1.1b) was replaced by $-U$, was analyzed in [27]. These results were extended in [4], where the predator-prey type police interaction as given in (1.1b) was considered for the regime $D = \mathcal{O}(\varepsilon^{-2})$. One key result of these studies was the identification of a Hopf bifurcation for steady-state hotspot patterns that leads to asynchronous oscillations in the amplitudes of the hotspots. This initial instability effectively displaces crime between adjacent spatial regions, as consistent with that observed in certain field studies [2]. More recently, in [21] a weakly nonlinear analysis of the three-component RD model, using an alternative dimensionless formulation to (1.1) and in the non-singular limit, was implemented to characterize the bifurcation properties of the spatially uniform steady-state. For a certain parameter regime, this rigorous analysis established the existence of a Hopf bifurcation that initiates large-scale pattern formation and the oscillations that occur far from the spatially uniform state. Numerical computations in [21] have illustrated that, in the fully nonlinear regime, (1.1) can exhibit a wide range of highly complex spatio-temporal hotspot patterns that await a theoretical understanding.

We will analyze the steady-state and linear stability of crime hotspots that occur for (1.1) in the singular limit $\varepsilon \ll 1$, but where $D = \mathcal{O}(1)$. By focusing on the asymptotic regime $D = \mathcal{O}(1)$, our main goal is to hopefully incorporate into a single scaling regime two distinct competing mechanisms that we conjecture to be

3

key ingredients for producing complex spatio-temporal dynamics of hotspot patterns; one mechanism to annihilate hotspots and a further mechanism to nucleate new hotspots from a quiescent background. For the two-component RD urban crime model without police, it was shown in [26] that when $D = \mathcal{O}(1)$ new hotspots of criminal activity can nucleate from a crime-free quiescent background as a consequence of a saddle-node bifurcation point of hotspot equilibria. For the three-component model (1.1), but in the scaling regime $D = \mathcal{O}(\varepsilon^{-2}) \gg 1$, hotspot nucleation behavior does not occur. Instead, it was shown in [4] from a nonlocal eigenvalue problem (NLEP) linear stability analysis that, on a certain range of D, the linearization of a steady-state multi-hotspot pattern can undergo a Hopf bifurcation as τ is increased, which leads to asynchronous temporal oscillations in the hotspot amplitudes. Since the police diffusivity is $D_p = D/\tau$, this regime occurs when the police response is sufficiently sluggish with D_p below a threshold. Full numerical computations in [4] have suggested that if this oscillatory instability is unstable it typically will lead to a non-monotonic annihilation of certain hotspots in the pattern.

Undertaking a steady-state and linear stability analysis of hotspot patterns for (1.1) when $D = \mathcal{O}(1)$ is much more intricate than for the $D = \mathcal{O}(\varepsilon^{-2})$ regime studied in [4] and the $D = \mathcal{O}(1)$ regime for the two-component model with no police studied in [26]. One key challenge for constructing hotspot steady-states for (1.1) with $D = \mathcal{O}(1)$ in the singular limit $\varepsilon \to 0$ is to analyze the effect of certain nonlocal terms. Our analysis will show that saddle-node bifurcations still occur for steady-state solutions even in the presence of police, and that the oscillatory instabilities of the hotspot amplitudes discovered in [4] still persist in this new scaling regime.
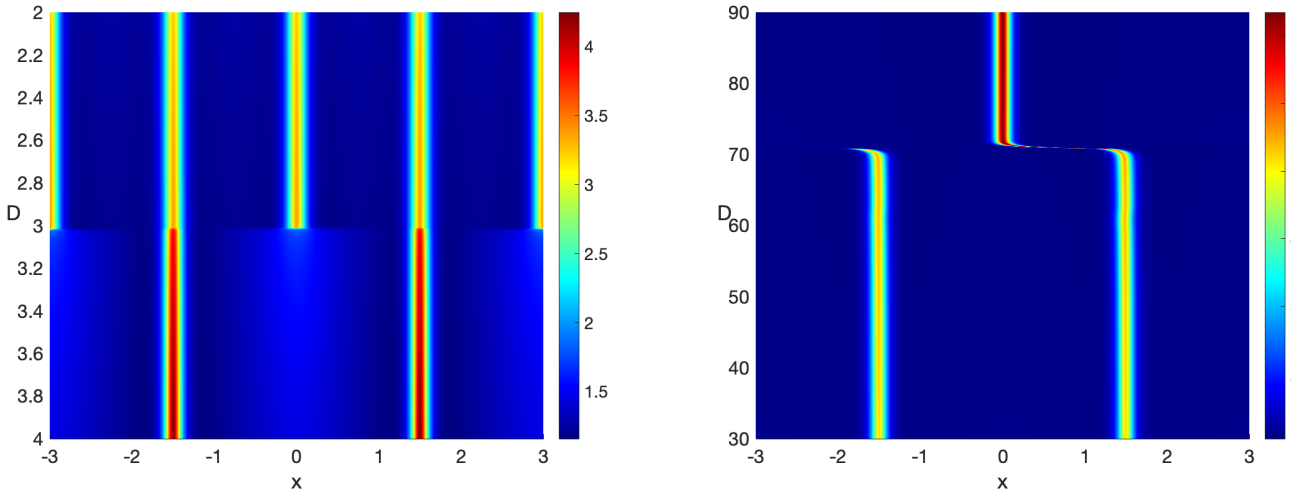

Figure 2: Left: Hotspot nucleation process as D is slowly decreased in time with $D = 4 - 10^{-5}t$; Right: A competition instability as D is increased leading to the monotonic collapse of a hotspot with $D = 30 + 10^{-5}t$. The colormap based on the amplitude of A is shown as D is changed. See Appendix C for movies of these processes. Parameters: $\alpha = 1$, $\gamma = 2$, $\varepsilon = 0.05$, $q = 3$, $U_0 = 5$, $L = 3$ and $\tau = 1$.

From numerical simulations of (1.1) we now illustrate a few dynamical processes that can occur for hotspot patterns of (1.1) when $\varepsilon \to 0$ and $D = \mathcal{O}(1)$. Firstly, new hotspots of criminal activity can be nucleated in low crime regions when the criminal diffusivity D is decreased. This process is illustrated in the left panel of Figure 2 for an initial condition consisting of a two-hotspot steady-state solution to (1.5) when D is varied in time as $D = 4 - 10^{-5}t$. As D is gradually decreased, the initial pattern becomes unstable and new hotspots are nucleated at the domain boundary and in between two adjacent hotspots. For the same parameter set, but where D is gradually increased in time as $D = 30 + 10^{-5}t$, in the right panel of Figure 2 we show the monotonic collapse of one hotspot in the multi-hotspot pattern as D increases past a threshold D_c. The surviving hotspot then undergoes a slow subsequent drift towards its steady-state location. This phenomenon is referred to as competition instability. Finally, when τ is large enough and when $D < D_c$, Figure 3 shows that the two-hotspot
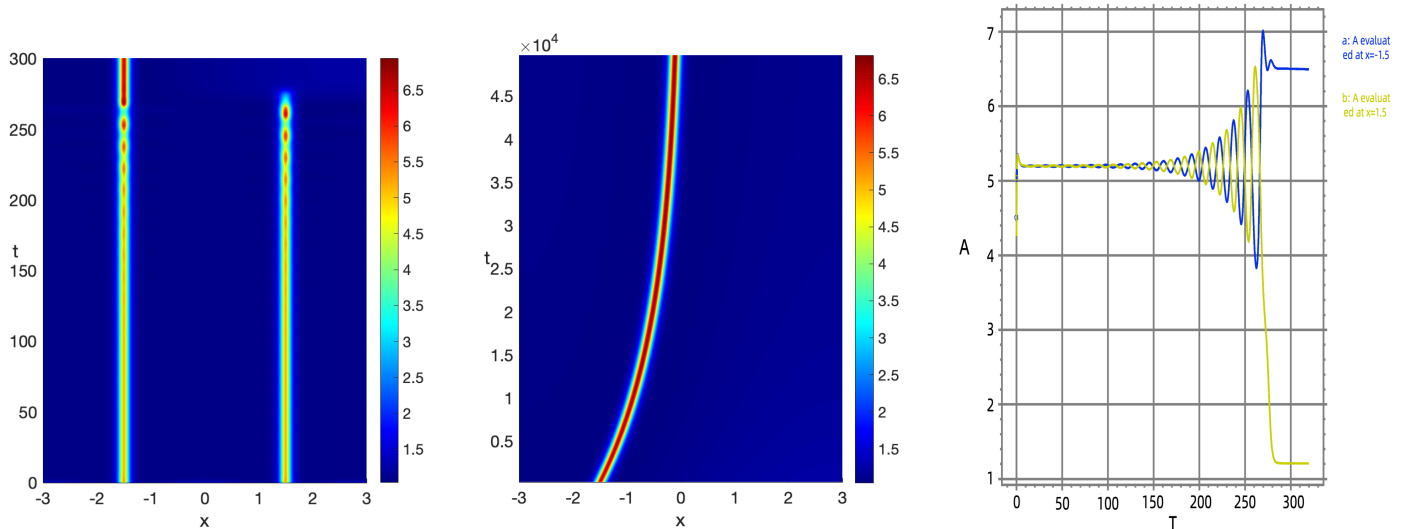
4

Figure 3: Annihilation of hotspots arising from an asynchronous oscillatory instability. Left: Asynchronous oscillatory instabilities of hotspot amplitudes occur when τ exceeds a Hopf bifurcation boundary. Middle: Long time behaviour of the remaining hotspot. Right: The spot amplitudes of A at $x = \pm 1.5$ computed numerically from the full PDE system (1.1). See Appendix C for a movie of the oscillatory collapse. Parameters: $\alpha = 1$, $\gamma = 2$, $\varepsilon = 0.05$, $q = 3$, $U_0 = 5$, $L = 3$, $\tau = 10$ and $D = 60$.

steady-state is unstable to an asynchronous oscillatory instability of the hotspot amplitudes, which ultimately annihilates one of the hotspots in an oscillatory collapse. The surviving hotspot then drifts over a very long time period towards the domain midpoint. Movies of these three processes are given in Appendix C.

To identify parameter ranges where both hotspot nucleation and asynchronous hotspot amplitude oscillations can be coincident in the $D = \mathcal{O}(1)$ regime, we will focus on a specific two-boundary hotspot pattern. For this pattern we will provide a phase diagram in the τ versus D parameter plane where distinctly different hotspot dynamics can occur. In one region of this phase diagram, we show that the combined effect of hotspot nucleation and annihilation can lead to persistent large scale oscillations of the hotspot amplitudes, which we refer to as *nucleation-annihilation* dynamics. Moreover, by using translation invariance and symmetry, we show that the phase diagram for this canonical two-boundary hotspot pattern still applies to some multi-hotspot patterns that replicate the two-boundary hotspot pattern. This is illustrated in Figure 4, where a multi-hotspot pattern that replicates the two-boundary hotspot pattern three times is shown to exhibit nucleation-annihilation dynamics at a predicted point in the linear stability phase diagram of the canonical two-boundary hotspot pattern. Based on our detailed case study of two-boundary hotspot patterns, and together with a few further numerical experiments, we conjecture that nucleation-annihilation dynamics are a key mechanism for generating complex spatio-temporal hotspot dynamics for (1.1). Overall, our proposed mechanism is reminiscent of the merging-emerging dynamics uncovered in [16] and [9] for the 1-D Keller-Segel chemotaxis model with logistic growth. In these studies it was shown that the dynamical pair-wise merging of localized peaks, together with their nucleation from a quiescent background via a Turing instability whenever the inter-peak separation exceeded a threshold, were the underlying mechanisms for highly irregular, but persistent, spatio-temporal dynamics.

The outline of this paper is as follows. In §2 we use a formal singular perturbation analysis in the limit $\varepsilon \to 0$ to construct hotspot steady-state solutions to (1.5). For the steady-state problem, (1.1) reduces to a singularly perturbed nonlocal two-component boundary-value problem (BVP). Based largely on the derivation of a new explicit formula for the homoclinic connection characterizing the hotspot profile, we provide asymptotic
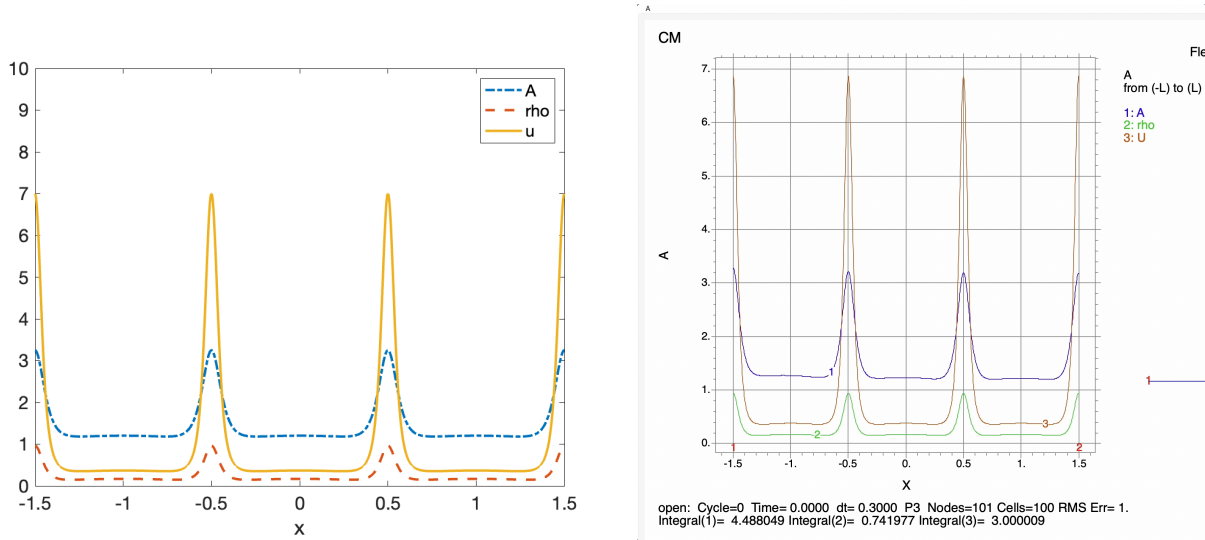
5

Figure 4: A multi-hotspot steady-state that consists of three replicates of the canonical two-boundary hotspot pattern in Figure 11 with parameters $\alpha = 1$, $\gamma = 2$, $\varepsilon = 0.03$, $q = 3$, $L = 3$ and $U_0 = 3$, which must be three times as large as the value $U_0 = 1$ used for the canonical phase diagram in the right panel of Figure 11. Left: hotspot steady-state when $D = 1.7$. Right: Full PDE simulations showing nucleation-annihilation dynamics for the indicated point in the shaded Region A of the phase diagram in Figure 11 where $D = 1$ and $\tau = 40$.

predictions for the steady-state hotspot amplitude that are rather accurate even for only moderately small ε. When the police deployment U_0 is below a threshold, hotspot steady-state solutions are shown to exist provided that $D > D_{crit,\varepsilon}$. This critical value is the minimum value of D at which the outer limit of the steady-state solution exists, and is found to closely approximate a saddle-node bifurcation point for the existence of hotspot steady-states. Near this critical value of D, hotspots are nucleated from a quiescent background. In §3 we provide a higher order analysis, extending and improving that in [26] for the case of no police, to obtain an accurate asymptotic prediction of the hotspot nucleation threshold $D_{crit,\varepsilon}$ when $U_0 \geq 0$. This analysis relies on a normal form equation derived in [12] in the study of self-replication behavior of mesa patterns. In §3 we also present global bifurcation branches of hotspot equilibria as computed using the continuation software *pde2path* [29].

In §4 we study the linear stability of two specific steady-state hotspot patterns. For a one-hotspot steady-state solution, we derive an NLEP that has three distinct nonlocal terms. From a numerical study of this NLEP we show that one-hotspot steady-states are always linearly stable. For a two-boundary hotspot steady-state solution, in §4.3 we numerically solve the eigenvalue problem for the linearization to construct a linear stability phase diagram in the τ versus D parameter space that delineates ranges of parameters where dynamically distinct solution behaviors. The behavior of the spectrum of the linearization as we cross stability boundaries is illustrated. Nucleation-annihilation dynamics, resulting in large-scale persistent oscillations of the hotspot amplitudes, is found to occur in one region of this phase diagram. Finally, in §5 we remark on some possible implications of our study, and we discuss a few problems that warrant further investigation.

2   The Steady State Hotspot Solution

In this section, we study the steady-state problem for (1.5) in the limit $\varepsilon \to 0$. To construct a K-hotspot steady-state solution with $K \geq 1$, we use the method of matched asymptotic expansions and follow the approach in [26]. That is, we first construct a single hotspot solution centered at $x = 0$ on $(-l, l)$ such that $l = L/K$. We

6

then apply a "gluing" technique to determine K-hotspot steady-states. The steady-state problem for (1.5) on the canonical domain $|x| \le l$, with no-flux conditions $A_x = V_x = u_x = 0$ at $x = \pm l$, is

$$\varepsilon^2 A_{xx} - A + VA^3 + \alpha = 0\,, \tag{2.1a}$$

$$D(A^2 V_x)_x - VA^3 + \gamma - \alpha - uVA^{2+q} = 0\,, \tag{2.1b}$$

$$D(A^q u_x)_x = 0\,. \tag{2.1c}$$

From integrating (2.1c) with $u_x(\pm l) = 0$, we find that u is a constant. By using $U = uA^q$ and (1.3), we get

$$u = \frac{U_0}{\int_{-L}^{L} A^q\, dx} = \frac{U_0}{K \int_{-l}^{l} A^q\, dx}\,, \tag{2.2}$$

where U_0 is the constant total police deployment. In this way, the three-component steady-state problem (2.1) reduces to the following two-component, but nonlocal, BVP:

$$\varepsilon^2 A_{xx} - A + VA^3 + \alpha = 0\,, \quad |x| \le l\,; \qquad A_x(\pm l) = 0\,, \tag{2.3a}$$

$$D(A^2 V_x)_x - VA^3 + \gamma - \alpha - \frac{U_0}{K \int_{-l}^{l} A^q\, dx} VA^{2+q} = 0\,, \quad |x| \le l\,; \qquad V_x(\pm l) = 0\,. \tag{2.3b}$$

This system has a similar structure to the steady-state problem in [26] but it contains an extra nonlocal term, which makes the analysis much more intricate than in [26]. A naive asymptotic analysis would be to let $A \sim A_0/\varepsilon = \mathcal{O}(\varepsilon^{-1})$ in the hotspot inner region, which has the effect of neglecting the α term in (2.3a) to leading order. Upon doing so, this makes the homoclinic solution satisfy $A_0(y) \to 0$ as $y \to \infty$, where $y \equiv x/\varepsilon$ [26]. However, this leading order analysis is not sufficiently accurate for evaluating the non-local term $\int_{-l}^{l} A^q\, dx$. As such, we must develop a more sophisticated approach than in [26] to construct the hotspot steady-state that is based on a more accurate determination of the homoclinic profile. In this more refined approach, we will construct a solution with $A = \mathcal{O}(1)$ in the inner region, but where A will ultimately depend weakly on ε.

We first introduce the inner variable $y = x/\varepsilon$ in (2.3) to obtain on $-\infty < y < \infty$ that

$$A_{yy} - A + VA^3 + \alpha = 0\,, \tag{2.4a}$$

$$D(A^2 V_y)_y = \varepsilon^2 \left(VA^3 - (\gamma - \alpha) + \frac{U_0}{K \int_{-l}^{l} A^q\, dx} VA^{2+q} \right)\,. \tag{2.4b}$$

By expanding $A \sim A_0 + \varepsilon A_1 + \dots$ and $V \sim V_0 + \varepsilon^2 V_1 + \dots$, we obtain from (2.4b) that, to leading order, $V = V_0$ is a constant to be determined. Upon setting

$$A_0(y) = \frac{w(y)}{\sqrt{V_0}}\,, \tag{2.5}$$

we obtain from (2.4a) that $w(y)$ is the homoclinic solution to

$$w_{yy} - w + w^3 + b = 0\,, \quad w(0) > 0\,, \quad w_y(0) = 0\,, \quad \text{where} \quad b \equiv \alpha\sqrt{V_0} > 0\,. \tag{2.6}$$

In Appendix A we derive the following new explicit result for the existence of a homoclinic solution to (2.6):

Lemma 1 *For $0 \le b < b_c \equiv \frac{2}{3\sqrt{3}}$, there is a unique homoclinic solution $w(y)$ to (2.6) given explicitly by*

$$w(y) = \frac{c(y)(1 - 2w_\infty^2) + w_\infty}{1 + c(y)w_\infty}\,, \quad \text{where} \quad c(y) \equiv \sqrt{\frac{2}{1 - w_\infty^2}}\, \text{sech}(\sqrt{1 - 3w_\infty^2}\, y)\,. \tag{2.7}$$

Here $w_\infty > 0$ is the smallest positive root of $w^3 - w + b = 0$. The homoclinic solution satisfies $w(y) \to w_\infty$ as $|y| \to \infty$. We have $b < w_\infty < 3b/2$ and that $w_\infty \to 0$ as $b \to 0$. In the limit $b \to 0$, we recover the usual leading order profile $w = \sqrt{2}\, \text{sech}(y)$ as in [26]. In terms of w_∞, we have $w(0) \equiv w_m = -w_\infty + \sqrt{2}(1 - w_\infty^2)^{1/2}$.

7

Proof 1 *The explicit homoclinic profile (2.7) is derived in Appendix A. To show that w_∞ lies on the range $b < w_\infty < 3b/2$, we use $b = \alpha\sqrt{V_0} > 0$ and set $w_\infty = nb > 0$ in $w^3 - w + b = 0$ to obtain that n satisfies*

$$B(n) \equiv \frac{n-1}{n^3} = b^2 > 0\,. \tag{2.8}$$

For $b \to 0$, we have $n \to 1$, so that $w_\infty \sim b$. We calculate $B(1) = 0$ and $B'(n) = n^{-4}(3 - 2n)$, so that $B'(n) > 0$ on $1 \le n < 3/2$. Since $B(3/2) = 4/27 = b_c^2$, we conclude by the monotonicity of $B(n)$ that for any b in $0 < b < b_c$, the minimal root of (2.8) must satisfy $1 < n < 3/2$, which establishes that $b < w_\infty < 3b/2$. As a result, if we define $A_{0\infty} \equiv \lim_{y\to\infty} A_0(y)$, we have that $A_{0\infty}$ satisfies

$$\alpha < A_{0\infty} \equiv \frac{w_\infty}{\sqrt{V_0}} < \frac{3\alpha}{2}\,. \tag{2.9}$$

Remark 1 *In our analysis below, we will derive a nonlinear algebraic equation for V_0, which will show that $V_0 \ll 1$ as $\varepsilon \to 0$ but with an intricate dependence on ε. This will yield that $b = \alpha\sqrt{V_0} \ll 1$ as $\varepsilon \to 0$. However, by including the effect of b in the non-perturbative explicit expression (2.7) we retain a highly accurate approximation for the homoclinic solution. In this way, we avoid having to construct additional nested inner layers as was done in §5 of [26] in the absence of police, where the analysis there was instead based on perturbing around the leading order homoclinic profile $w = \sqrt{2}\,\mathrm{sech}(y)$. One key finding of [26] was that a mid-inner boundary layer with $y = \mathcal{O}(-\log\varepsilon)$ is needed to match the inner solution to an outer solution. As a consequence, the outer solution was defined on the renormalized domain $x_\varepsilon < x < l$, where $x_\varepsilon \equiv -\varepsilon\log\varepsilon$ (see §5 of [26]). Although our explicit formula for the homoclinic avoids the need to introduce nested inner layers, the fact that $b \ll 1$ indicates that we should still use the renormalized outer domain $x_\varepsilon < x < l$ in our analysis below.*

We now analyze (2.3) on the renormalized outer region $-l < x < -x_\varepsilon$ and $x_\varepsilon < x < l$. Since the hotspot solution is even, we only consider the range $x_\varepsilon < x < l$. On this range, the leading order outer solution is

$$A \sim a_0(x)\,, \qquad V \sim v_0(x)\,, \tag{2.10}$$

where $a_0(x)$ and $v_0(x)$ satisfy

$$D(a_0^2 v_{0x})_x - v_0 a_0^3 + \gamma - \alpha - \frac{U_0}{KI} v_0 a_0^{q+2} = 0\,, \qquad v_0 = g(a_0) \equiv \frac{a_0 - \alpha}{a_0^3}\,. \tag{2.11}$$

Here we have labeled $I \equiv 2\int_0^l A^q\, dx$. To match a_0 and v_0 to the inner solution, we require that

$$a_0(x_\varepsilon) = A_{0\infty} = w_\infty/\sqrt{V_0}\,, \qquad v_0(x_\varepsilon) = V_0\,. \tag{2.12}$$

From Lemma 1, we observe that $a_0(x_\varepsilon)$ satisfies $\alpha < a_0(x_\varepsilon) < 3\alpha/2$.

By substituting $v_0 = g(a_0)$ into the first equation in (2.11), we obtain the following BVP on $x_\varepsilon < x < l$:

$$D(f(a_0)a_{0x})_x = R(a_0) \equiv a_0 - \gamma + \frac{U_0}{KI}(a_0 - \alpha)a_0^{q-1}\,; \qquad a_0(x_\varepsilon) = \frac{w_\infty}{\sqrt{V_0}}\,, \quad a_{0x}(l) = 0\,. \tag{2.13}$$

Here we have defined $f(a_0)$ by

$$f(a_0) \equiv \frac{3\alpha - 2a_0}{a_0^2} = a_0^2 g'(a_0)\,. \tag{2.14}$$

For the well-posedness of (2.13), we need $f(a_0) > 0$ on $x_\varepsilon < x < l$. A sufficient condition for this to hold is that $a_0(x_\varepsilon) < a_0(x) < 3\alpha/2$.

8

To ensure this range for $a_0(x)$, we will now derive a sufficient condition for $a_0(x)$ to be monotone increasing. To do so, we need to analyze $R(a_0)$ in (2.13). We calculate that $R(\alpha) = \alpha - \gamma < 0$ and that

$$R'(a_0) = 1 + \frac{U_0}{KI} q a_0^{q-2} \left(a_0 - \alpha + \frac{\alpha}{q} \right) > 0 \,, \tag{2.15}$$

for $a_0 > \alpha$. Therefore, since $\alpha < a_0(x_\varepsilon)$, we have $R(a_0) < 0$ on the interval $a_0(x_\varepsilon) < a_0(x) < 3\alpha/2$ when $R(3\alpha/2) < 0$. By using the expression for $R(a_0)$ in (2.13), we observe that $R(3\alpha/2) < 0$ holds provided that the total police deployment U_0 satisfies

$$U_0 < U_{0,max} \equiv 2 \left(\frac{2}{3} \right)^{q-1} \frac{(\gamma - 3\alpha/2)}{\alpha^q} KI \,, \tag{2.16}$$

where $I = 2 \int_0^l A^q \, dx$. Observe that $U_{0,max} > 0$ since $\gamma > 3\alpha/2$ from (1.2). The inequality (2.16) provides a maximum threshold for the total level of police deployment for which steady state hotspot solutions can exist. We will assume below that there are limited police resources so that (2.16) is satisfied.

Under the condition (2.16), which establish that $R(a_0) < 0$ on $a_0(x_\varepsilon) < a_0 < 3\alpha/2$, it follows that a_0 is monotone increasing on $x_\varepsilon < x < l$. To see this, we integrate (2.13) and use $a_{0x}(l) = 0$ to get

$$Df(a_0)a_{0x} \Big|_x^l = -Df(a_0)a_{0x} = \int_x^l R(a_0(s)) \, ds \,.$$

Since $R(a_0) < 0$ and $f(a_0) > 0$ on $\alpha < a_0(x_\varepsilon) < a_0 < 3\alpha/2$, we conclude that $a_{0x} > 0$ on this range.

Next, we reduce (2.13) to a simple quadrature by multiplying both sides of (2.13) by $f(a_0)a_{0x}$ and integrating the resulting expression using the boundary condition $a_{0x}(l) = 0$. This yields that

$$\frac{D}{2}(f(a_0)a_{0x})^2 = \int_l^x f(a_0(\eta)) R(a_0(\eta)) a_{0\eta} \, d\eta \,. \tag{2.17}$$

Upon labeling $\mu \equiv a_0(l)$, and using the monotonicity of a_0, we conclude that

$$\frac{D}{2}(f(a_0)a_{0x})^2 = \int_\mu^{a_0(x)} f(s)R(s) \, ds = G(\mu; z) - G(a_0; z) \,, \tag{2.18}$$

where we have defined the anti-derivative G, upon using (2.13) for R, by

$$G'(s; z) = -f(s)R(s) \equiv f(s) \left(\gamma - s - z(s - \alpha)s^{q-1} \right) \,, \quad \text{where} \quad z \equiv \frac{U_0}{KI} \,. \tag{2.19}$$

After substituting $f(s)$ from (2.14) into (2.19) and integrating once, we obtain that $G(s; z)$ is given explicitly by

$$G(s; z) = 2s - (2\gamma + 3\alpha) \log(s) - \frac{3\alpha\gamma}{s} + z \left(\frac{2s^q}{q} - \frac{5\alpha s^{q-1}}{q-1} + \left\{ \begin{array}{ll} 3\alpha^2 \log(s) & \text{if } q = 2 \\ 3\alpha^2 \frac{s^{q-2}}{q-2} & \text{if } q \neq 2 \end{array} \right. \right) \,. \tag{2.20}$$

Since $f(a_0) > 0$ and $R(a_0) < 0$ on $a_0(x_\varepsilon) < a_0 < 3\alpha/2$, it follows that $G'(s; z) > 0$ on this range so that the inequality $G(\mu; z) - G(a_0; z) > 0$ is guaranteed. As a result, since $a_{0x} > 0$, we obtain from (2.18) that

$$f(a_0)a_{0x} = \sqrt{\frac{2}{D}} \sqrt{G(\mu; z) - G(a_0; z)} \,. \tag{2.21}$$

By integrating the separable ODE (2.21) we get

$$\chi(a_0(x); z) = \sqrt{\frac{2}{D}} (x - x_\varepsilon) \,, \qquad \text{where} \qquad \chi(a_0(x); z) \equiv \int_{a_0(x_\varepsilon)}^{a_0(x)} \frac{f(s)}{\sqrt{G(\mu; z) - G(s; z)}} \, ds \,. \tag{2.22}$$

9

Then, by setting $x = l$ and $a_0(l) = \mu$ we obtain an implicit equation for $\mu \equiv a_0(l)$ given by

$$\sqrt{\frac{2}{D}}(l - x_\varepsilon) = \chi(\mu; z) = \int_{a_0(x_\varepsilon)}^{\mu} \frac{f(s)}{\sqrt{G(\mu; z) - G(s; z)}}\, ds\,, \qquad \text{where} \quad a_0(x_\varepsilon) = \frac{w_\infty}{\sqrt{V_0}}\,. \tag{2.23}$$

Since the integral in (2.23) is improper at $s = \mu$, to obtain a more tractable formula for $\chi(\mu; z)$ we integrate it by parts by using $f(s) = -G'(s)/R(s)$. In this way, we can determine $\chi(\mu; z)$ in terms of a proper integral as

$$\chi(\mu; z) = -\frac{2\sqrt{G(\mu; z) - G(a_0(x_\varepsilon); z)}}{R\left(a_0(x_\varepsilon)\right)} + 2\int_{a_0(x_\varepsilon)}^{\mu} \frac{\sqrt{G(\mu; z) - G(s; z)}}{\left(R(s)\right)^2}\left(1 + z\left(qs^{q-1} - \alpha(q-1)s^{q-2}\right)\right)\, ds\,, \tag{2.24}$$

where $R(s) \equiv s - \gamma + z(s - \alpha)s^{q-1}$ with $z \equiv U_0/(KI)$.

We observe that $\chi(a_0; z)$ is positive and monotonically increasing in a_0 since $\chi'(a_0; z) = \frac{f(a_0)}{\sqrt{G(\mu; z) - G(a_0; z)}} > 0$ for $U_0 < U_{0,max}$. Since $\mu = a_0(l) \leq 3\alpha/2$, the largest possible value of μ is $3\alpha/2$, and so we define χ_{max} by

$$\chi_{max} \equiv \chi\left(3\alpha/2; z\right)\,. \tag{2.25}$$

Upon fixing l, we conclude from (2.23) that the minimum value $D_{crit,\varepsilon}$ of D for which an outer solution exists is

$$D_{crit,\varepsilon} = \frac{2(l - x_\varepsilon)^2}{\chi_{max}^2}\,, \qquad \text{where} \quad x_\varepsilon \equiv -\varepsilon \log \varepsilon\,. \tag{2.26}$$

Finally, we must determine V_0 by matching the behavior of V in the inner and outer regions. To do so, we first expand $V = V_0 + \varepsilon^2 V_1 + \ldots$ in the inner region and collect $\mathcal{O}(\varepsilon^2)$ terms in (2.4) to obtain that V_1 satisfies

$$D(A_0^2 V_{1y})_y = V_0 A_0^3 - (\gamma - \alpha) + zV_0 A_0^{2+q}\,, \qquad \text{where} \qquad z = \frac{U_0}{K \int_{-l}^{l} A^q\, dx}\,. \tag{2.27}$$

By using the expression $A_0 = w(y)/\sqrt{V_0}$ for the homoclinic we get

$$\frac{D}{V_0}(w^2 V_{1y})_y = H(y)\,, \quad 0 < y < \infty; \qquad H(y) \equiv \frac{1}{\sqrt{V_0}}w^3(y) - (\gamma - \alpha) + \frac{z}{V_0^{q/2}}w^{2+q}(y)\,. \tag{2.28}$$

To match to the outer solution, we need the far-field behavior of V_1 in (2.28) as $y \to \infty$. Since $\int_0^\infty H(y)\, dy$ does not exist owing to the fact that $H(\infty) \neq 0$, we rewrite the right-hand side of (2.28) by adding and subtracting $H(\infty)$. Then, upon integrating (2.28) for V_1 and imposing the symmetry condition $V_{1y}(0) = 0$, we obtain

$$\frac{D}{V_0}w^2 V_{1y} = \int_0^y \left(H(s) - H(\infty)\right)\, ds + yH(\infty); \qquad H(\infty) \equiv \frac{1}{\sqrt{V_0}}w_\infty^3 - (\gamma - \alpha) + \frac{z}{V_0^{q/2}}w_\infty^{2+q}\,. \tag{2.29}$$

Since $w(y) \to w_\infty$ exponentially as $y \to +\infty$, we conclude that $\int_0^\infty \left(H(s) - H(\infty)\right)\, ds < \infty$. By letting $y \to \infty$ in (2.29), we obtain the far field behavior

$$V_{1y} \sim \frac{V_0}{Dw_\infty^2}\left(c_0 + c_1 y\right)\,, \quad \text{as} \quad y \to +\infty\,, \tag{2.30}$$

where the constants c_0 and c_1 are given explicitly by

$$c_0 \equiv \int_0^\infty \left(H(y) - H(\infty)\right)\, dy = \frac{1}{\sqrt{V_0}}\int_0^\infty \left(w^3(y) - w_\infty^3\right)\, dy + \frac{z}{V_0^{q/2}}\int_0^\infty \left(w^{2+q}(y) - w_\infty^{2+q}\right)\, dy\,, \tag{2.31a}$$

$$c_1 \equiv H(\infty; z) = \frac{1}{\sqrt{V_0}}w_\infty^3 - (\gamma - \alpha) + \frac{z}{V_0^{q/2}}w_\infty^{2+q}. \tag{2.31b}$$

10

Next we study the behavior as $x \to x_\varepsilon$ of the outer solution $v_0(x)$. From (2.11), we find that $v_0(x)$ satisfies

$$D(a_0^2 v_{0x})_x = v_0 a_0^3 - (\gamma - \alpha) + z v_0 a_0^{q+2}, \qquad (2.32)$$

with $v_0(x_\varepsilon) = V_0$ and $v_{0x}(l) = 0$. Since $a_0(x_\varepsilon) = w_\infty / \sqrt{V_0}$, we obtain from (2.32) that

$$v_{0xx}(x_\varepsilon) \sim \frac{V_0}{D w_\infty^2} \left(\frac{1}{\sqrt{V_0}} w_\infty^3 - (\gamma - \alpha) + \frac{z}{V_0^{q/2}} w_\infty^{2+q} \right). \qquad (2.33)$$

Then, by expanding $v_{0x}(x)$ in a Taylor series we get

$$v_{0x}(x) = v_{0x}(x_\varepsilon) + (x - x_\varepsilon) v_{0xx}(x_\varepsilon) + \ldots = v_{0x}(x_\varepsilon) - x_\varepsilon v_{0xx}(x_\varepsilon) + v_{0xx}(x_\varepsilon) x + \ldots \quad \text{as} \quad x \to x_\varepsilon, \qquad (2.34)$$

where $x_\varepsilon \equiv -\varepsilon \log(\varepsilon)$. Now we enforce a continuity condition between (2.34) and (2.30). After using $V_y = \varepsilon V_x$, and $V \sim V_0 + \varepsilon^2 V_1$, we obtain from (2.30) that

$$v_{0x}(x) = \frac{1}{\varepsilon} V_y \sim \varepsilon V_{1y} = \varepsilon \frac{c_0 V_0}{D w_\infty^2} + \frac{c_1 V_0}{D w_\infty^2} x. \qquad (2.35)$$

We observe from (2.31b) and (2.33) that the second term in (2.35) matches identically with the $v_{0xx}(x_\varepsilon)$ term in (2.34). Therefore, to ensure that the other terms agree, we must have

$$v_{0x}(x_\varepsilon) - x_\varepsilon v_{0xx}(x_\varepsilon) = \varepsilon \frac{c_0 V_0}{D w_\infty^2}. \qquad (2.36)$$

Next, by using (2.11) for v_0 and (2.21) we calculate

$$v_{0x} = \frac{1}{a_0^2} \left(f(a_0) a_{0x} \right) = \frac{1}{a_0^2} \sqrt{\frac{2}{D}} \sqrt{G(\mu; z) - G(a_0; z)}. \qquad (2.37)$$

Since $a_0(x_\varepsilon) = A_{0\infty} = \frac{w_\infty}{\sqrt{V_0}}$ we conclude that

$$v_{0x}(x_\varepsilon) = \frac{V_0}{w_\infty^2} \sqrt{\frac{2}{D}} \sqrt{G(\mu; z) - G(A_{0\infty}; z)}. \qquad (2.38)$$

Finally, by substituting (2.31a), (2.33) and (2.38) into (2.36), we obtain that V_0 must satisfy

$$\frac{1}{\sqrt{V_0}} \int_0^\infty \left(w^3 - w_\infty^3 \right) dy + \frac{z}{V_0^{q/2}} \int_0^\infty \left(w^{2+q} - w_\infty^{2+q} \right) dy = \frac{1}{\varepsilon} \sqrt{2D} \sqrt{G(\mu; z) - G(A_{0\infty}; z)}$$

$$- \frac{x_\varepsilon}{\varepsilon} \left(\frac{1}{\sqrt{V_0}} w_\infty^3 - (\gamma - \alpha) + \frac{z}{V_0^{q/2}} w_\infty^{2+q} \right), \qquad (2.39)$$

where $x_\varepsilon \equiv -\varepsilon \log(\varepsilon)$. The final step in the derivation of the equation for V_0 is to approximate the integral $I \equiv 2 \int_0^l A^q dx$, which determines z by $z = U_0/(KI)$. Since $q > 1$, the dominant contribution to I arises from the inner region, and we can approximate I as

$$I \sim 2 \int_0^l (A^q - A_{0\infty}^q) \, dx + 2l A_{0\infty}^q = 2V_0^{-q/2} \left(\varepsilon J_q + l w_\infty^q \right), \qquad \text{where} \qquad J_q \equiv \int_0^\infty (w^q - w_\infty^q) \, dy, \qquad (2.40)$$

which yields

$$z \sim \frac{U_0}{2K} \left(\frac{V_0^{q/2}}{\varepsilon J_q + l w_\infty^q} \right). \qquad (2.41)$$

11

With this approximation, (2.39) yields a nonlinear algebraic equation for V_0

$$\frac{\varepsilon}{\sqrt{V_0}} J_3 + x_\varepsilon \left(\frac{w_\infty^3}{\sqrt{V_0}} - (\gamma - \alpha) + \frac{U_0}{2\varepsilon K} \frac{w_\infty^{2+q}}{(J_q + l w_\infty^q / \varepsilon)} \right) + \frac{U_0}{2K} \frac{J_{2+q}}{(J_q + l w_\infty^q / \varepsilon)} = \sqrt{2D} \sqrt{G(\mu; z) - G(A_{0\infty}; z)} = 0 \,.$$
$$(2.42)$$

In (2.42) we have defined the generic integral J_p by $J_p \equiv \int_0^\infty (w^p(y) - w_\infty^p)\, dy$. From (2.42) we observe that formally $V_0 = \mathcal{O}(\varepsilon^2)$, but that the dependence on ε is rather intricate.
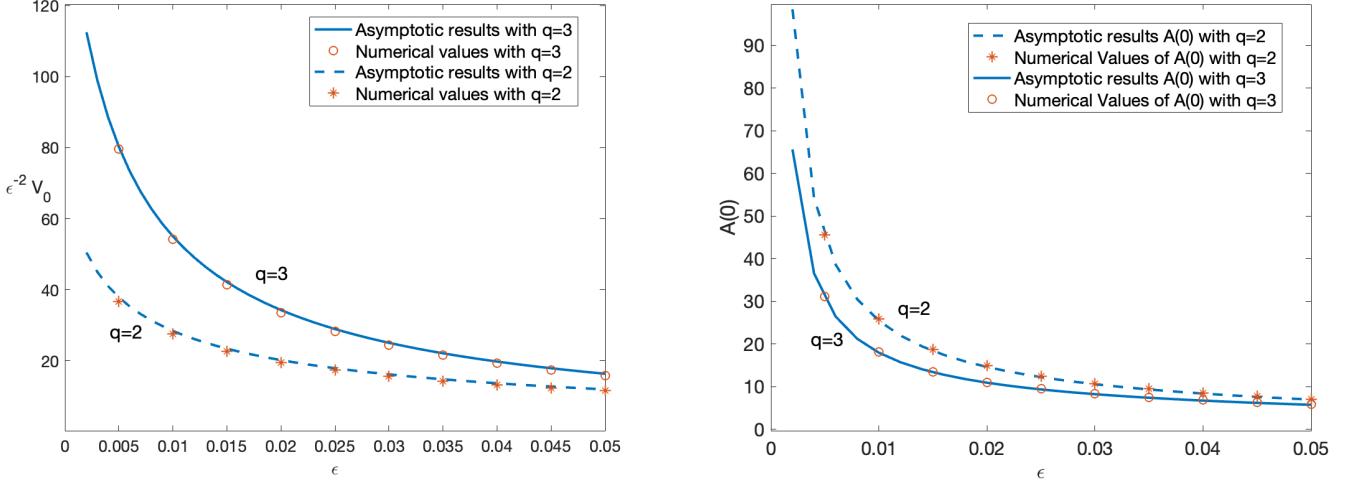

Figure 5: Comparison between numerical and asymptotic results for $\varepsilon^{-2} V_0$ (left panel) and for $A(0)$ (right panel). The solid and dashed curves correspond to the asymptotic results with $q = 3$ and $q = 2$, respectively, as computed from the nonlinear algebraic system (2.42) and (2.23). The circle and star points are obtained by numerical simulations of (1.1) with $q = 3$ and $q = 2$, respectively. There is very close agreement between the asymptotic and numerical results up to $\varepsilon = 0.05$. Parameters: $l = 1$, $\alpha = 1$, $\gamma = 2$, $D = 5$, $K = 1$ and $U_0 = 1$.

2.1 Numerical verification

In this subsection we verify our asymptotic results for the hotspot steady state with full numerical simulations of (1.1) by *FlexPDE* [6] for $q = 3$ and for the "cops on the dots" case where $q = 2$. We observe that (2.42) is a highly implicit nonlinear algebraic equation for V_0 owing to the following features:

- $w(y)$ depends on V_0 through b in (2.6), with the leading order behavior $w \sim \sqrt{2}\mathrm{sech}(y)$ and $w_\infty = \lim_{y\to\infty} w(y) \sim \alpha \sqrt{V_0}$ as $V_0 \to 0$.

- z as given in (2.41) depends on V_0 and appears in the function $G(s; z)$ of (2.20).

- $J_p \equiv \int_0^\infty (w^p(y) - w_\infty^p)\, dy$ is integrable for integers $p > 1$ (see the details for analytically calculating J_p in Appendix B), but these integrals depend on V_0. Note that by using $w_\infty^3 - w_\infty + b = 0$, we can rewrite (2.6) as $w_{yy} - (w - w_\infty) + (w^3 - w_\infty^3) = 0$. As a result, by integrating over $0 < y < \infty$ we get $J_1 = J_3$.

- (2.42) contains $\mu = a_0(l)$, which is given by (2.23) and it depends on z and V_0.

Since the equations (2.42) and (2.23) form a coupled system for the unknowns V_0 and μ, which contains the terms w_∞, z, J_p that depend on V_0, we solve for V_0 and μ numerically using Newton's method. In Figure 5, we show a very close agreement between the scaled asymptotic results $\varepsilon^{-2} V_0$ (left panel) and hotspot height
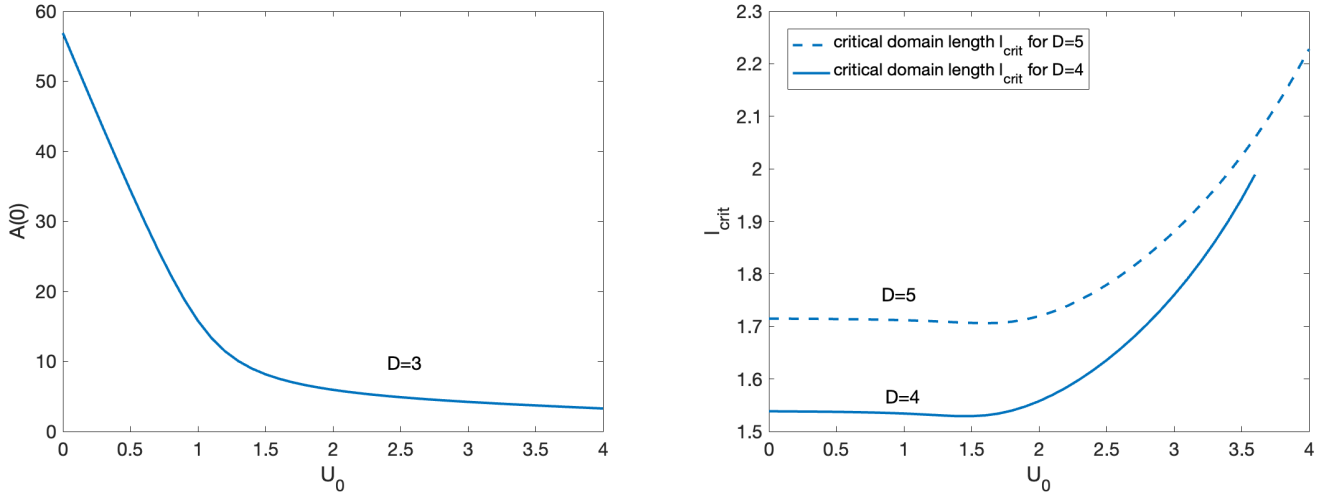
12

Figure 6: The effect of U_0 on the hotspot height $A(0)$ (left) and the critical value of domain length l_{crit} (right) for which hotspot nucleation will occur when $l > l_{crit}$. Parameters: $l = 1$, $\alpha = 1$, $\gamma = 2$, $q = 3$, $U_0 = 1$, $K = 1$, and $\varepsilon = 0.01$, with D as indicated.

$A(0)$ (right panel) with corresponding full simulation results of (1.1) computed using *FlexPDE* [6]. These plots show that, for the choices $q = 3$ and $q = 2$ of police drift, the asymptotic results predict with high accuracy the full numerical results over the full range $0 < \varepsilon < 0.05$. In contrast, in the absence of police, the asymptotic approach in [26] based on perturbing from the leading order homoclinic solution for the hotspot profile provided a substantially poorer approximation for $\varepsilon^{-2}V(0)$ when $\varepsilon \geq 0.02$ (see the right panel of Figure 4 of [26]).

To determine how the total police deployment U_0 affects the hot-spot steady state, in the left panel of Figure 6 we plot the hotspot height $A(0)$ versus U_0 in the range $U_0 \in [0, 4]$. This plot shows that the existence of police can effectively reduce the attractiveness of the environment to burglary. Moreover, we investigate how l_{crit}, defined as the critical value of the domain size for which new hotspots of criminal activity will be nucleated when $l > l_{crit}$, depends on U_0. Qualitatively, the critical distance $2l_{crit}$ represents the maximum inter-hotspot separation that can occur before a new hotspot will be nucleated at the midpoint between adjacent hotspots. In the right panel of Figure 6 we plot l_{crit} versus U_0, as computed from (2.26) for a fixed D. This plot shows, as expected intuitively, that with an increase in police deployment U_0 there can be a larger inter-hotspot separation where no nucleation of new hotspots of criminal activity can occur. We remark that in both panels of Figure 6, $A(0)$ and l_{crit} may not exist when the police deployment U_0 is too large. When U_0 is too large, the outer solution no longer exists and steady-state hotspot patterns cannot form.

As we now remark, our detailed construction of a one-hotspot steady-state also applies to multi-hotspot steady-states by using translation symmetry and glueing to ensure a C^2 global solution.

Remark 2 *To apply our one-hotspot steady-state results to a K-hotspot steady-state we simply set $l = L/K$ in calculating the saddle-node threshold $D_{crit,\varepsilon}$ from (2.26) and (2.42). For a K-hotspot steady-state, and for D near the resulting saddle-node threshold, we predict that hotspot nucleation will occur at the spatial midpoint between two adjacent interior hotspots or on the domain boundaries at $x = \pm L$, owing to reflection through the Neumann boundary conditions. This hotspot nucleation behavior is analyzed in detail from a normal form analysis in §3.*

13

3 Global Bifurcation Structure and the Onset of Nucleation

In this section we numerically compute global bifurcation diagrams of hotspot steady-state solutions, and we provide a more refined asymptotic theory than given in §2 to analyze the onset of nucleation behavior that occurs when $l \approx l_{crit,\varepsilon}$, or equivalently when $D \approx D_{crit,\varepsilon}$, where $D_{crit,\varepsilon}$ is given in (2.26). Recall that $D_{crit,\varepsilon}$ denotes the minimum value of D for which a single hotspot steady-state will exist on the domain $|x| \leq l$, while $l_{crit,\varepsilon}$ is the maximum value of l for which a hotspot steady-state exists when the criminals have diffusivity D.

3.1 Global bifurcation structure

To compute global bifurcation diagram of hotspot steady-state solutions we use *FlexPDE* [6] and *pde2path*[29, 18] and we compare the full numerical results with the asymptotic result for the critical value $D_{crit,\varepsilon}$ derived in (2.26). These computations give a detailed view on how new hotspots are created near the endpoints $x = \pm l$ when D approaches a bifurcation point, which we denote by D_{num}. In Figure 7, we show the full numerical bifurcation results of (1.5) for single-hotspot steady states computed using *pde2path*. The vertical axis on the bifurcation diagrams (a) and (c) is the boundary value $A(l)$, and the horizontal axis is D. Panel (b) and (d) are plots of attractiveness $A(x)$ at marked points in (a) and (c). The parameter values are $q = 3, K = 1, U_0 = 1, \gamma = 2, \alpha = 1, l = 1$, with $\varepsilon = 0.03$ in the top panels (a), (b) and $\varepsilon = 0.04$ in the bottom panels (c), (d). Both bifurcation diagrams (a) and (c) show that starting from the bottom solution branch, the steady-state solution branch with one interior hotspot becomes unstable as D is decreased below the circled point D_{num}. This branch is connected to a solution that has an interior hotspot together with a hotspot at each boundary. To show this, in panels (b) and (d) we plot the continuation of steady states by choosing a few points along the branch, where we observe that new hotspots of criminal activity can be nucleated at the domain boundary.

The global bifurcation numerical results at the circled points shown in Figure 7 are verified with a full simulation of (1.1) using *FlexPDE*, where we numerically compute time-dependent simulations of (1.1) as D is gradually decreased until hotspot nucleation behavior is observed. From these simulations, we estimate that

$$D_{num} = 1.493 \quad \text{for} \quad \varepsilon = 0.03, \quad D_{num} = 1.434 \quad \text{for} \quad \varepsilon = 0.04,$$

which are exactly the circled points in Figure 7. Moreover, we compare the bifurcation points with the fold points shown in Figure 7 (a), (c). This is shown in Figure 8, where the blue solid line corresponds to bifurcation points, denoted by D_{num}, and the purple dotted line corresponds to the fold points, denoted by D_{fold}. It is observed that D_{num} and D_{fold} approach each other as $\varepsilon \to 0$.

Next, we compare the leading order approximation $D_{crit,\varepsilon}$ derived in (2.26) with full simulation results. Recall that $\chi(\mu; z)$ reaches its maximum at $\mu = \frac{3}{2}\alpha$ which determines χ_{max} from (2.25). Moreover, it contains z, which relates to V_0. To compute $D_{crit,\varepsilon}$, we fix $\mu = \frac{3}{2}\alpha$ and compute V_0 and $D_{crit,\varepsilon}$ simultaneously by applying Newton's method. The result is shown in Figure 8, where the red dashed curve is the asymptotic result $D_{crit,\varepsilon}$ obtained from (2.26) by varying ε from 0.01 to 0.04, and the blue curve is obtained from full simulations using *FlexPDE*. From 8 we observe that this leading order prediction for the critical value of D is rather inaccurate unless ε is very small, while for larger ε it has the wrong qualitative dependence on ε. This motivates the need for a higher-order asymptotic theory to characterize the onset of hotspot nucleation.

To provide a more accurate analytical theory for the onset of hotspot nucleation near $x = \pm l$, we must construct a new boundary layer solution near the endpoints $x = \pm l$ when D is near the critical value $D_{crit,\varepsilon}$. This leading order critical value was derived from the outer problem for $a_\varepsilon(x)$ given by

$$D\left[f(a_\varepsilon)a_{\varepsilon x}\right]_x = a_\varepsilon - \gamma + \frac{U_0}{KI}(a_\varepsilon - \alpha)a_\varepsilon^{q-1}, \quad x_\varepsilon < x < l; \qquad a_\varepsilon(x_\varepsilon) = \frac{w_\infty}{\sqrt{V_0}} \quad a_{\varepsilon x}(l) = 0, \qquad (3.1)$$

where $f(a_0)$ is given in (2.14), $I = 2\int_0^l A^q dx \sim 2V_0^{-q/2}(\varepsilon J_q + lw_\infty^q)$, and $x_\varepsilon \equiv -\varepsilon \log(\varepsilon)$.
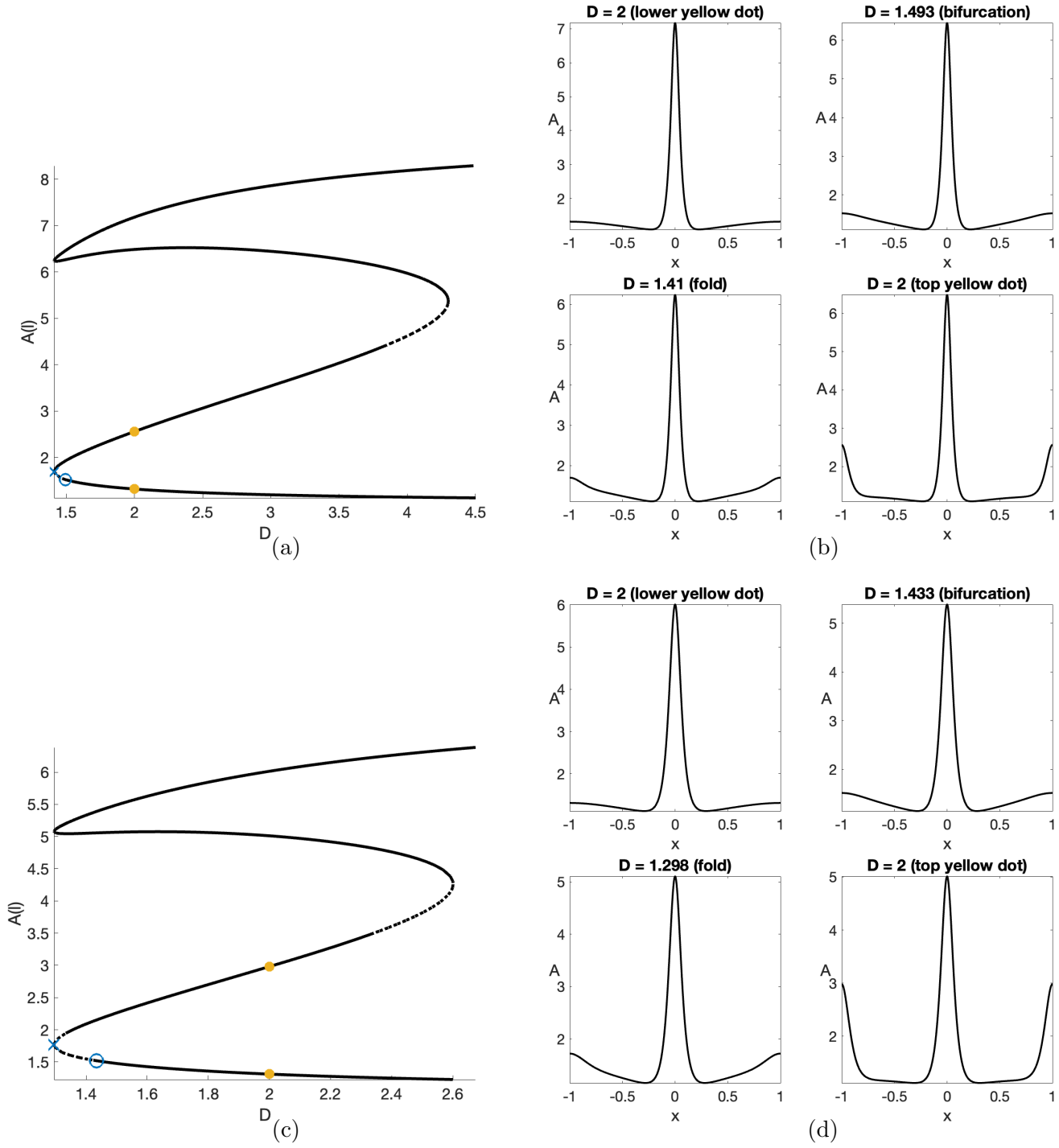
14

Figure 7: Continuation of steady states starting with single-hotspot for $l = 1$, $\alpha = 1$, $\gamma = 2$, $q = 3$ and $U_0 = 1$. Panel (a) and (c) are bifurcation diagrams obtained by *pde2path* [29] with $\varepsilon = 0.03$ and $\varepsilon = 0.04$, respectively. The circle corresponds to the bifurcation point D_{num} at which the interior-hotspot pattern becomes unstable. The cross corresponds to a fold point which is connected to a solution that has an interior hotspot together with a hotspot at each boundary. Panel (b) and (d) show the profile of the attractiveness A at various values of D specified on top. These values of D correspond to the marked points on the bifurcation diagram (left figure).
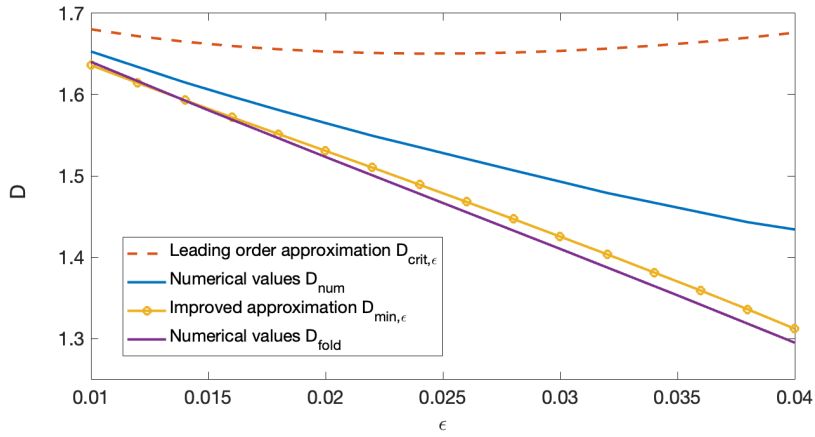
15

Figure 8: Comparison between asymptotic and numerical results for the critical value of D at the onset of nucleation. The solid blue curve, denoted as D_{num}, is obtained from full time-dependent simulations of (1.1) by *FlexPDE*. The red dashed curve is the leading order approximation $D_{crit,\varepsilon}$ given in (2.26). The yellow dotted curve is the improved approximation in (3.25) that corresponds to $D_{min,\varepsilon}$, in which H_l is computed in Table 1. This curve closely approximates the purple dotted curve that corresponds to the fold points of the bifurcation diagrams of Figure 7 as computed using *pde2path* [29]. Parameters: $l = 1$, $\alpha = 1$, $\gamma = 2$, $q = 3$ and $U_0 = 1$.

To illustrate how our previous analysis becomes invalid near the onset of nucleation, we determine the local behavior near $x = l$ of the solution to (3.1) when $D = D_{crit,\varepsilon}$, which corresponds to setting $a_\varepsilon(l) = a_{0c} = 3\alpha/2$. Near $x = l$, we put $a_\varepsilon = a_{0c} + \bar{a}(x)$, where $\bar{a} \ll 1$ and $\bar{a}(l) = 0$. Upon substituting this into (3.1), we integrate once while using $\bar{a}(l) = 0$ to obtain for x near l that

$$\left(\frac{1}{2}\bar{a}^2\right)_x \sim \beta a_{0c}^2(x - l)\,, \qquad \text{where} \qquad \beta \equiv \frac{\left(\gamma - a_{0c} - z(a_{0c} - \alpha)a_{0c}^{q-1}\right)}{2D_{crit,\varepsilon}}\,, \quad \text{and} \quad z = \frac{U_0}{KI}\,. \qquad (3.2)$$

Upon integrating (3.2) and imposing $\bar{a}(l) = 0$, we obtain that $\bar{a} \sim \sqrt{\beta}a_{0c}(x - l)$ as $x \to l^-$. Therefore, the local behavior of the solution a_ε when $D = D_{crit,\varepsilon}$ is

$$a_\varepsilon(x) \sim a_{0c} + \sqrt{\beta}a_{0c}(x - l)\,, \quad \text{as} \quad x \to l^-\,. \qquad (3.3)$$

From (3.3), we conclude that when $D = D_{crit,\varepsilon}$ and $a_\varepsilon(l) = 3\alpha/2$, the solution $a_\varepsilon(x)$ no longer satisfies the required no-flux condition $a_{\varepsilon x}(l) = 0$. This local analysis suggests that we need to construct a new boundary layer near $x = l$ to characterize the onset of nucleation.

3.2 The solution structure near the onset of nucleation

In this subsection, we construct a new boundary layer solution that characterizes the onset of hotspot nucleation that occurs near the endpoints $x = \pm l$ when D is near the critical value $D_{crit,\varepsilon}$. The overall analysis is similar to that done in [26] for the two-component urban crime model in the absence of police. In particular, we derive a normal form equation that has the same qualitative structure as that derived in [26], [12], but where the improved prediction for the nucleation threshold value of D now depends on the police deployment U_0.

To analyze the onset of nucleation, we first write (2.3) on $x_\varepsilon < x < l$ in the form

$$\varepsilon^2 A_{xx} + A^3(V - g(A)) = 0\,, \qquad D\left[A^2V_x\right]_x - A + \gamma - A^3(V - g(A)) - zVA^{2+q} = 0\,, \qquad (3.4)$$

16

where $g(A) = (A - \alpha)/A^3$, $z = U_0/(KI)$ and $I = \int_{-l}^{l} A^q \, dx$. We let $a_\varepsilon(x)$ and $D_{crit,\varepsilon}$ denote the solution to the renormalized outer problem (3.1) at the critical value where $a_\varepsilon(l) = 3\alpha/2$ and $v_\varepsilon(x) = g(a_\varepsilon(x))$. In the outer region, defined away from both the hotspot core and a new thin boundary layer to be constructed near $x = l$, we expand the outer solution as

$$A = a_\varepsilon + \nu a_{\varepsilon,1} + \dots, \qquad V = v_\varepsilon + \nu v_{\varepsilon,1} + \dots, \qquad \Lambda \equiv \frac{1}{D} = \Lambda_\varepsilon + \nu \Lambda_{\varepsilon,1} + \dots, \tag{3.5}$$

where the gauge function $\nu \ll 1$ and the constant $\Lambda_{\varepsilon,1}$ are to be determined. By expanding $D = D_{crit,\varepsilon} + \nu D_{\varepsilon,1} + \dots$ and comparing it with the expansion of Λ, we conclude that

$$D_{crit,\varepsilon} = \frac{1}{\Lambda_\varepsilon}, \qquad D_{\varepsilon,1} = -\frac{\Lambda_{\varepsilon,1}}{\Lambda_\varepsilon^2}. \tag{3.6}$$

Our focus below is to calculate the correction term $D_{\varepsilon,1}$ for the critical value of the diffusivity threshold.

To do so, we first substitute (3.5) into (3.4) and collect powers of ν. Assuming that $\nu \gg \mathcal{O}(\varepsilon^2)$, we obtain that the leading order term a_ε satisfies the renormalized problem (3.1), while at the next order $a_{\varepsilon,1}$ satisfies

$$[f(a_\varepsilon)a_{\varepsilon,1}]_{xx} - \Lambda_\varepsilon a_{\varepsilon,1} \left(1 + z \left(g(a_\varepsilon)a_\varepsilon^{2+q} \right)_{a_\varepsilon} \right) = \Lambda_{\varepsilon,1} \left(a_\varepsilon - \gamma + z(a_\varepsilon - \alpha)a_\varepsilon^{q-1} \right), \tag{3.7}$$

on the domain $x_\varepsilon < x < l$ with $a_{\varepsilon,1}(x_\varepsilon) = 0$ and where, from (2.14), we have $f(a_\varepsilon) \equiv (3\alpha - 2a_\varepsilon)/a_\varepsilon^2$. Our local analysis below will provide the required asymptotic boundary condition for $a_{\varepsilon,1}$ as $x \to l^-$.

Near $x = l$, we construct a thin boundary layer by introducing the new variables $\mathcal{A}_1, \mathcal{V}_1$, and s by

$$A = a_{0c} + \delta \mathcal{A}_1(s) + \dots, \qquad V = v_{0c} + \delta^2 \mathcal{V}_1(s) + \dots, \qquad s \equiv \frac{l - x}{\sigma}, \tag{3.8}$$

where $a_{0c} \equiv 3\alpha/2$ and $v_{0c} \equiv g(a_{0c}) = 4/(27\alpha^2)$. The gauge functions $\delta \ll 1$ and $\sigma \ll 1$ are to be determined. The choice of different scales for A and V is due to the fact that $g'(a_{0c}) = 0$. We substitute (3.8) into (3.4) and perform a Taylor expansion of $g(A)$ around a_{0c} to obtain that

$$\frac{\varepsilon^2 \delta}{\sigma^2} \mathcal{A}_{1ss} + \delta^2 a_{0c}^3 \left[\mathcal{V}_1 - \frac{1}{2} \mathcal{A}_1^2 g''(a_{0c}) \right] + \dots = 0, \qquad \frac{\delta^2}{\sigma^2} a_{0c}^2 \mathcal{V}_{1ss} = \Lambda_\varepsilon \left[a_{0c} - \gamma + z v_{0c} a_{0c}^{2+q} \right] + \dots, \tag{3.9}$$

where from (2.11) for v_0 we compute $g''(a_{0c}) = -2a_{0c}^{-4}$, with $a_{0c} = 3\alpha/2$.

To balance the terms in (3.9), we must choose the scales $\delta = \sigma = \varepsilon^{2/3}$. Then, upon using $v_{0c} = g(a_{0c}) = (a_{0c} - \alpha)/a_{0c}^3$, we obtain to leading order that (3.9) becomes

$$\mathcal{A}_{1ss} + a_{0c}^3 \left[\mathcal{V}_1 - \frac{1}{2} \mathcal{A}_1^2 g''(a_{0c}) \right] = 0, \qquad \mathcal{V}_{1ss} = -\frac{2\beta}{a_{0c}^2}, \quad \text{where} \quad \beta = \frac{\Lambda_\varepsilon \left(\gamma - a_{0c} - z(a_{0c} - \alpha)a_{0c}^{q-1} \right)}{2}. \tag{3.10}$$

Since A and V have no-flux boundary conditions at $x = l$, we must impose that $\mathcal{A}_{1s}(0) = \mathcal{V}_{1s}(0) = 0$. By solving for $\mathcal{V}_1$ in (3.10) with $\mathcal{V}_{1s}(0) = 0$, we obtain that

$$\mathcal{V}_1 = \mathcal{V}_{10} - \beta \frac{s^2}{a_{0c}^2}, \tag{3.11}$$

where $\mathcal{V}_{10}$ is an arbitrary constant. Upon substituting $\mathcal{V}_1$ into the $\mathcal{A}_1$ equation of (3.10), we get

$$\mathcal{A}_{1ss} + a_{0c}^3 \left(\frac{\mathcal{A}_1^2}{a_{0c}^4} - \frac{\beta}{a_{0c}^2} s^2 + \mathcal{V}_{10} \right) = 0, \qquad 0 < s < \infty. \tag{3.12}$$

17

To obtain the *core problem*, as introduced in [26], [12], we simply rescale s and $\mathcal{A}_1$ by

$$\mathcal{A}_1 = bU, \quad s = \xi y, \qquad \text{where} \qquad b = a_{0c}\beta^{1/3}, \quad \xi = \beta^{-1/6}. \tag{3.13}$$

In this way, (3.12) transforms to the *core problem* [12]:

$$U_{yy} + U^2 - y^2 + k = 0, \quad 0 < y < \infty, \quad U_y(0) = 0; \qquad k \equiv a_{0c}^2\beta^{-2/3}\mathcal{V}_{10}. \tag{3.14}$$

In terms of the original variables, we obtain from (3.8), and (3.13) that the boundary layer solution near $x = l$, characterizing the onset of the nucleation of a hotspot, is given by the local solution

$$A \sim a_{0c} + \varepsilon^{2/3}a_{0c}\beta^{1/3}U(y), \qquad V \sim v_{0c} + \varepsilon^{4/3}\frac{\beta^{2/3}}{a_{0c}^2}(k - y^2), \qquad y \equiv \beta^{1/6}\varepsilon^{-2/3}(l - x), \tag{3.15}$$

where $a_{0c} = 3\alpha/2$, $v_{0c} = g(a_{0c}) = 4/(27\alpha^2)$, and β is given in (3.10). In terms of the outer coordinate, we have

$$A_x = -a_{0c}\beta^{1/2}U_y. \tag{3.16}$$

Therefore, upon matching to the local behavior as $x \to l$ of the outer solution $a_\varepsilon(x)$, as given by (3.3), we must have $U_y \to -1$ as $y \to \infty$.

We observe that $-U$ is the solution to the equation (3.4) in [12], where its solution behavior was established rigorously in Theorem 2 of [12]. We summarize this previous result for the convenience of the reader.

Theorem 1 *(From [12]) In the limit $k \to -\infty$, (3.14) admits exactly two solutions $U = U^\pm(y)$ with $U' > 0$ for $y > 0$, with the following uniform expansions:*

$$U^+ \sim -\sqrt{y^2 - k}, \qquad U^+(0) \sim -\sqrt{-k}, \tag{3.17}$$

$$U^- \sim -\sqrt{y^2 - k}\left(1 - 3\operatorname{sech}^2\left(\frac{\sqrt{-k}y}{\sqrt{2}}\right)\right), \quad U^-(0) \sim 2\sqrt{-k}. \tag{3.18}$$

These two solutions are connected. For any such solution, let $s \equiv U(0)$ and consider the solution branch $k = k(s)$. Then, $k(s)$ has a unique (maximum) critical point at $s = s_{max}$ and $k = k_{max}$. Numerical computations yield that $k_{max} \approx 1.46638$ and $s_{max} \approx 0.61512$.

We now proceed to compute the higher order correction term $D_{\varepsilon,1}$ to $D_{crit,\varepsilon}$. To do so, we need to derive the asymptotic boundary condition for $a_{\varepsilon,1}$ as $x \to l^-$. This analysis is similar to that for no police (see [26]).

Any solution to (3.14) with $U_y \to -1$ as $y \to \infty$ has asymptotics

$$U \sim -\sqrt{y^2 - k} + \mathcal{O}(y^{-4}) \sim -y + \frac{k}{2y} + \mathcal{O}(y^{-2}). \tag{3.19}$$

By substituting (3.19) into (3.15) and matching with the outer solution $a_{\varepsilon,1}(x)$ given in (3.7), we conclude that

$$\nu \equiv \varepsilon^{4/3}, \qquad \text{and} \qquad a_{\varepsilon,1} \sim \left(\frac{a_{0c}k\beta^{1/6}}{2}\right)\frac{1}{l - x}, \qquad \text{as} \quad x \to l^-. \tag{3.20}$$

To solve (3.7) subject to (3.20), it is convenient to introduce the new variable $\tilde{a}_{\varepsilon,1}$ defined by $\tilde{a}_{\varepsilon,1} \equiv f(a_\varepsilon)a_{\varepsilon,1}$. Therefore, as $x \to l^-$, we have upon using $f(a_{0c}) = 0$, $f'(a_{0c}) = -2/a_{0c}^2$, and (3.3) that

$$\tilde{a}_{\varepsilon,1} = f(a_\varepsilon)a_{\varepsilon,1} \sim \left(f(a_{0c}) + f'(a_{0c})a_{0c}\beta^{1/2}(x - l)\right)\left(\frac{a_{0c}k\beta^{1/6}}{2}\right)\frac{1}{l - x} = \beta^{2/3}k. \tag{3.21}$$

18

In this way, we conclude by setting $\tilde{a}_{\varepsilon,1} \equiv f(a_\varepsilon)a_{\varepsilon,1}$ in (3.7), and using (3.21), that $\tilde{a}_{\varepsilon,1}$ satisfies

$$\left(\tilde{a}_{\varepsilon,1}\right)_{xx} - \frac{\Lambda_\varepsilon}{f(a_\varepsilon)}\left(1 + z\left(g(a_\varepsilon)a_\varepsilon^{2+q}\right)_{a_\varepsilon}\right)\tilde{a}_{\varepsilon,1} = \Lambda_{\varepsilon,1}\left(a_\varepsilon - \gamma + z(a_\varepsilon - \alpha)a_\varepsilon^{q-1}\right), \qquad x_\varepsilon < x < l\,, \tag{3.22a}$$

$$\tilde{a}_{\varepsilon,1}(x_\varepsilon) = 0\,, \qquad \tilde{a}_{\varepsilon,1} \sim \beta^{2/3}k \quad \text{as} \quad x \to l^-\,. \tag{3.22b}$$

We observe that (3.22) reduces to equation (5.51) of [26] when there is no police, i.e. when $z = 0$. Then, to determine $\Lambda_{\varepsilon,1}$ we introduce the new variable H by $\tilde{a}_{\varepsilon,1} \equiv \Lambda_{\varepsilon,1}H$, so that H satisfies

$$H_{xx} - \frac{\Lambda_\varepsilon}{f(a_\varepsilon)}\left(1 + z\left(g(a_\varepsilon)a_\varepsilon^{2+q}\right)_{a_\varepsilon}\right)H = a_\varepsilon - \gamma + z(a_\varepsilon - \alpha)a_\varepsilon^{q-1}\,, \qquad x_\varepsilon < x < l\,, \tag{3.23}$$

where $H(x_\varepsilon) = 0$ and H is bounded as $x \to l^-$ in the sense that $H_l \equiv \lim_{x\to l^-} H(x) \neq 0$. Here $a_\varepsilon(x)$ is the solution to (3.1) when $D = D_{crit,\varepsilon}$. In terms of the solution to (3.23) and the constant H_l, we identify that

$$\Lambda_{\varepsilon,1} = \frac{\beta^{2/3}k}{H_l}\,. \tag{3.24}$$

Finally, with the expression for β in (3.10), we obtain from (3.6), together with setting $x = l$ in (3.15), that the curve $A(l)$ versus D near the onset of nucleation can be parameterized as

$$D \sim D_{crit,\varepsilon} - \varepsilon^{4/3}D_{crit,\varepsilon}^2\beta^{2/3}\frac{k}{H_l}\,, \qquad A(l) \sim a_{0c} + \varepsilon^{2/3}a_{0c}\beta^{1/3}U(0)\,, \tag{3.25}$$

where $a_{0c} = 3\alpha/2$. The parameterization of this curve is in terms of the parameter k, as defined in the normal form (3.14). By solving (3.14) numerically in the left panel of Figure 9 we plot $U(0)$ in (3.25) in terms of k.
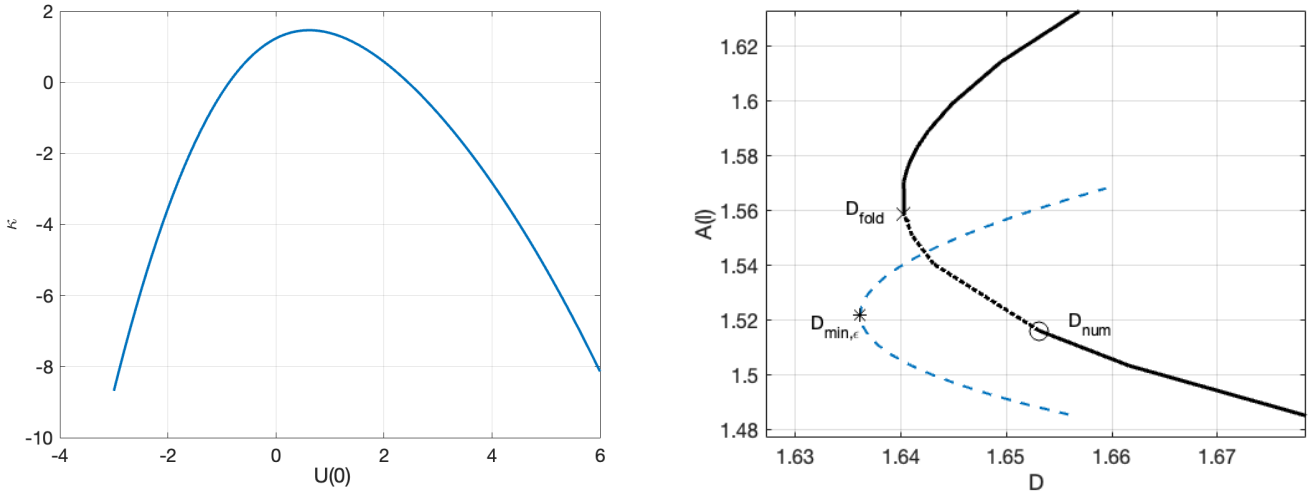

Figure 9: Left: Plot of the bifurcation diagram of k versus $U(0)$ as computed numerically from (3.14). Right: The asymptotic result (dashed curve) for $A(l)$ versus D very close to the fold point, as obtained from (3.25) with $H_l = 0.0583$, is compared with the corresponding full numerical result (solid curve) computed using *pde2path*. Parameters: $l = 1$, $\alpha = 1$, $\gamma = 2$, $\varepsilon = 0.01$ and $q = 3$.

The final step for implementing the parameterization (3.25) is to numerically compute the constant H_l from (3.23). To do so, we must first formulate an appropriate asymptotic boundary condition for H as $x \to l^-$. This

is done by differentiating $\tilde{a}_{\varepsilon,1} = f(a_\varepsilon)a_{\varepsilon,1}$, while using (3.3) together with the local behavior for $a_{\varepsilon,1}$ in (3.20). Upon Taylor expanding, and recalling that $f(a_{0c}) = 0$, we obtain for $x \to l^-$ that

$$\frac{d\tilde{a}_{\varepsilon,1}}{dx} = f'(a_\varepsilon)\frac{da_\varepsilon}{dx}a_{\varepsilon,1} + f(a_\varepsilon)\frac{da_{\varepsilon,1}}{dx} \sim \left(\frac{a_{0c}k\beta^{1/6}}{2}\right)\left[f'(a_\varepsilon)\sqrt{\beta}a_{0c} + \frac{f(a_\varepsilon)}{(l-x)^2}\right],$$

$$\sim \left(\frac{a_{0c}k\beta^{1/6}}{2}\right)\left[\left(f'(a_{0c}) + a_{0c}\sqrt{\beta}f''(a_{0c})\right)\frac{\sqrt{\beta}a_{0c}}{(l-x)} - \frac{\sqrt{\beta}a_{0c}}{(l-x)}f'(a_{0c})\right] \sim -\left(\frac{a_{0c}k\beta^{1/6}}{2}\right)a_{0c}^2\beta f''(a_{0c}).$$

As a result, since $f''(a_{0c}) = 8a_{0c}^{-3}$, we conclude that

$$\frac{da_{\varepsilon,1}}{dx} \sim -4\beta^{7/6}k, \quad \text{as} \quad x \to l^-. \tag{3.26}$$

Finally, we use $\tilde{a}_{\varepsilon,1} = \Lambda_{\varepsilon,1}H$, together with (3.24), to obtain the required asymptotic boundary condition

$$H'(x) \sim -4\sqrt{\beta}H(x), \quad \text{as} \quad x \to l^-, \tag{3.27}$$

where we identify that $H_l = H(l)$. Here β is given in (3.10).

To determine H_l, we use a shooting method on (3.23) that is based on iterating on the initial condition $H_0 \equiv H_x(x_\varepsilon)$ and then imposing (3.27) at $x = l - \delta$, where $0 < \delta \ll 1$. The function $a_\varepsilon(x)$ is solved numerically from (2.21) using *Matlab ODE113*. Numerical results for H_l at a few values of ε are given in Table 1.

ε	0.01	0.012	0.014	0.016	0.018	0.02	0.022	0.024
H_l	0.0538	0.0521	0.0506	0.0492	0.0480	0.0469	0.0459	0.0449
ε	0.026	0.028	0.03	0.032	0.034	0.036	0.038	0.04
H_l	0.0440	0.0432	0.0424	0.0417	0.0410	0.0404	0.0398	0.0392

Table 1: Calculation of H_l for different ε using a shooting method for the BVP (3.23) where the required condition (3.27) is imposed at $x = l - \delta$ with $\delta \ll 1$. Parameters: $l = 1$, $\alpha = 1$, $\gamma = 2$, $q = 3$ and $\delta = 0.004$.

Since $H_l > 0$ from Table 1, we conclude from (3.25) that the minimum value of D, which corresponds to the refined prediction for the saddle-node bifurcation point, is below the leading order threshold $D_{crit,\varepsilon}$ calculated from (2.26). Observe that D attains its minimum value $D_{min,\varepsilon}$ when $k = k_{max} \approx 1.46638$. Substituting H_l in Table 1 into (3.25), we get a much improved approximation of the saddle-node point for D at which hotspot nucleation is initiated. This is shown in Figure 8, where the yellow curve, corresponding to $D_{min,\varepsilon}$ obtained from (3.25), rather accurately predicts the saddle-node point computed from *pde2path* as ε is increased on the range $0.01 < \varepsilon < 0.04$. In the right panel of Figure 9 we show a decent comparison, in a zoomed plot, of the local approximation (3.25) of $A(l)$ versus D with *pde2path* numerical results.

4 Linear Stability Analysis of Steady State Hotspot Patterns

In this section we study the linear stability of steady-state hotspot solutions.

4.1 The NLEP for a single-hotspot solution

We first consider a single-hotspot steady-state solution on $|x| \leq l$ and we derive a nonlocal eigenvalue problem (NLEP) that characterizes its stability properties.

To formulate the NLEP we linearize around the steady state, denoted here by (A_e, V_e, u_e), by introducing

$$A = A_e + e^{\lambda t}\phi, \qquad V = V_e + e^{\lambda t}\psi, \qquad u = u_e + e^{\lambda t}\eta, \tag{4.1}$$

where $|\phi|, |\psi|, |\eta| \ll 1$. Upon substituting (4.1) into (1.5) we obtain that

$$\lambda\phi = \varepsilon^2 \phi_{xx} - \phi + 3V_e A_e^2 \phi + A_e^3 \psi \,, \tag{4.2a}$$

$$\lambda(2A_e V_e \phi + A_e^2 \psi) = D\left(2A_e V_{ex}\phi + A_e^2 \psi_x\right)_x - (3A_e^2 V_e + (2+q)u_e V_e A_e^{q+1})\phi$$
$$- (A_e^3 + u_e A_e^{2+q})\psi - V_e A_e^{2+q}\eta \,, \tag{4.2b}$$

$$\tau\lambda\left(qA_e^{q-1}u_e\phi + A_e^q\eta\right) = D\left(qA_e^{q-1}u_{ex}\phi + A_e^q\eta_x\right)_x \,, \tag{4.2c}$$

410 with $\phi_x = \psi_x = \eta_x = 0$ at $x = \pm l$. For $K = 1$, we recall from (2.2) and (2.41) that u_e is a constant, given by

$$u_e = \frac{U_0}{\int_{-l}^{l} A^q \, dx} \sim U_0\left(\frac{V_0^{q/2}}{\varepsilon \int_{-\infty}^{\infty}(w^q - w_\infty^q)\, dy + 2lw_\infty^q}\right)\,, \qquad \text{as} \quad \varepsilon \to 0\,. \tag{4.3}$$

411 To derive the NLEP we proceeds as follows. In the inner region we introduce the inner variable $y = x/\varepsilon$,
412 where the inner solutions for A_e and V_e are $A_e \sim w(y)/\sqrt{V_0}$ and $V_e \sim V_0$. Then, to leading order, (4.2b) and
413 (4.2c) yields $\psi_{yy} = 0$ and $\eta_{yy} = 0$, which have the bounded solutions $\eta \sim \eta(0) \equiv \eta_0$ and $\psi \sim \psi(0) \equiv \psi_0$, where
414 ψ_0 and η_0 are to be determined. Moreover, from (4.2a), we get that $\Phi(y) = \phi(\varepsilon y)$ satisfies

$$\Phi'' - \Phi + 3w^2\Phi + \frac{w^3}{V_0^{3/2}}\psi_0 = \lambda\Phi\,, \quad -\infty < y < \infty\,; \qquad \Phi \to 0 \quad \text{as} \quad |y| \to \infty\,. \tag{4.4}$$

415 The goal of the calculation below is to determine ψ_0, which will yield the NLEP from (4.4).

To do so, we first integrate (4.2c) over $|x| \le l$ and, by imposing $\eta_x(\pm l) = u_{ex}(\pm l) = 0$, we obtain that

$$qu_e \int_{-l}^{l} A_e^{q-1}\phi \, dx = -\int_{-l}^{l} A_e^q \eta \, dx\,. \tag{4.5}$$

416 Since $A_e = w/\sqrt{V_0}$ in the inner region where $w = \mathcal{O}(1)$ and $V_0 \ll 1$ while $A_e = a(x) = \mathcal{O}(1)$ in the outer region,
417 the main contribution for the integrals come from the inner region and we approximate the integrals in (4.5) only
418 over the hotspot region. Moreover, since $\int_{-\infty}^{\infty} w^p dy$ does not converge due to the fact that $\lim_{y\to\infty} w = w_\infty \ne 0$,
419 we must replace these integrals by the finite integral $\int_{-\infty}^{\infty}(w^p - w_\infty^p)\, dy$. In this way, to evaluate the integral on
420 the right hand side of (4.5), we first subtract and then add w_∞ to get

$$\int_{-\delta}^{\delta} w^p dx = \int_{-\delta}^{\delta}(w^p - w_\infty^p + w_\infty^p)\, dx = \varepsilon\int_{-\infty}^{\infty}(w^p - w_\infty^p)\, dy + 2\delta w_\infty^p \sim \varepsilon\int_{-\infty}^{\infty}(w^p - w_\infty^p)\, dy,$$

where δw_∞^p is ignored as $w_\infty \sim \alpha\sqrt{V_0} = \mathcal{O}(\varepsilon) \ll 1$. As a result, (4.5) becomes

$$\frac{qu_e}{V_0^{\frac{(q-1)}{2}}} \int_{-\infty}^{\infty} w^{q-1}\Phi \, dy \sim -\frac{\eta_0}{V_0^{q/2}} \int_{-\infty}^{\infty}(w^q - w_\infty^q)\, dy\,. \tag{4.6}$$

421 Upon defining the integrals J_p and I_p by

$$J_p \equiv \int_{-\infty}^{\infty}(w^p - w_\infty^p)\, dy\,, \qquad I_p \equiv \int_{-\infty}^{\infty} w^p\Phi \, dy\,, \tag{4.7}$$

422 we obtain from (4.6) that

$$\eta_0 \sim -qU_e V_0^{1/2}\frac{I_{q-1}}{J_q}\,. \tag{4.8}$$

423 Here for convenience J_p is re-defined as twice the integral used in the steady-state theory of §2 and Appendix B.

21

Next, we integrate the ψ-equation (4.2b) over $x \in (-l, l)$ where we impose $\psi_x(\pm l) = 0$. By using only the inner solutions to estimate the integrals, we obtain to leading order that

$$3I_2 + \frac{\psi_0}{V_0^{3/2}} J_3 + \frac{(2+q)}{V_0^{(q-1)/2}} u_e I_{q+1} + \frac{\eta_0}{V_0^{q/2}} J_{q+2} + \frac{\psi_0}{V_0^{1+q/2}} u_e J_{2+q} = -\lambda_0 \left(2V_0^{1/2} I_1 + \frac{\psi_0}{V_0} J_2 \right) . \tag{4.9}$$

Upon using (4.8) for η_0 and (4.3) for u_e, we obtain that (4.9) simplifies to

$$\frac{\psi_0}{V_0^{\frac{3}{2}}} \left(J_3 + \varepsilon^{-1}\sqrt{V_0}U_0 \frac{J_{2+q}}{J_q} + \lambda V_0^{1/2} J_2 \right) = -3I_2 - (2+q)\varepsilon^{-1}\sqrt{V_0}U_0 \frac{I_{q+1}}{J_q} - 2\lambda V_0^{1/2} I_1 - \frac{\eta_0}{V_0^{q/2}} J_{q+2} . \tag{4.10}$$

By dividing this expression by J_3, we obtain that

$$\frac{\psi_0}{V_0^{\frac{3}{2}}} (1 + K_q + \lambda B) = -\left(\frac{3I_2}{J_3} + (2+q)K_q \frac{I_{q+1}}{J_{q+2}} + 2\lambda B \frac{I_1}{J_2} - q K_q \frac{I_{q-1}}{J_q} \right) , \tag{4.11}$$

where we have defined B and K_q by

$$B \equiv V_0^{1/2} \frac{J_2}{J_3} , \qquad K_q \equiv \frac{V_0^{1/2} U_0}{\varepsilon J_3} \frac{J_{2+q}}{J_q} . \tag{4.12}$$

Finally, by substituting (4.11) into (4.4) and recalling the definitions of I_p and J_p in (4.7), we obtain

$$L_0 \Phi - w^3 \left(a(\lambda) \int w^2 \Phi + b(\lambda) \int w^{1+q} \Phi + c(\lambda) \int w^{q-1} + d(\lambda) \int w\Phi \right) = \lambda \Phi , \tag{4.13}$$

where $L_0 \Phi \equiv \Phi'' - \Phi + 3w^2 \Phi$ and the integrals are defined over $-\infty < y < \infty$. The λ-dependent multipliers are

$$a \equiv \frac{3}{J_3(1 + K_q + \lambda B)} , \quad b \equiv \frac{K_q(2+q)}{J_{2+q}(1 + K_q + \lambda B)} , \quad c \equiv -\frac{qK_q}{J_q(1 + K_q + \lambda B)} , \quad d \equiv \frac{2\lambda B}{J_2(1 + K_q + \lambda B)} .$$

For $q = 2$ and $q = 3$ the NLEP (4.13) has three distinct nonlocal terms. Moreover, since $V_0 = \mathcal{O}(\varepsilon^2)$, we can treat K_q in (4.12) as an $\mathcal{O}(1)$ parameter whose magnitude is proportional to the policing level U_0.

4.2 Numerical computations

Since the NLEP (4.13) is too complicated to analyze rigorously, we will determine the spectrum of the NLEP by using a finite difference approach. This leads to a nonlinear matrix eigenvalue problem in λ, where we seek to determine the eigenvalue with the largest real part using an iterative approach.

Since we are interested only in even solutions, we consider (4.13) on $(0, \infty)$. Since $w(y)$ decays exponentially to w_∞, we truncate the positive half-line to the large interval $y \in (0, L)$, where we chose $L = 20$. We discretize $\Phi(y_j) \sim \Phi_j$, where $y_j = j\Delta y$, for $j = 0, \ldots, N-1$ and $\Delta y = L/N - 1$, with $N = 300$. We use standard finite differences to approximate Φ'', while the midpoint rule is used to approximate the nonlocal integrals in (4.13). In this quadrature, the explicit form for the homoclinic w, as given in (2.7) of §2, was used. Recall that the integrals J_2, J_3, and J_4 can be calculated as in Appendix B.

With this discretization of the NLEP, we obtain the matrix eigenvalue problem $\mathcal{M}(\lambda)\Phi = \lambda\Phi$, where $\Phi \equiv (\Phi_1, \ldots, \Phi_N)^T$. As the entries in $\mathcal{M}$ depend on λ, we used an iterative approach for determining λ. Starting with some initial guess λ_0, we solve the standard matrix eigenvalue problem $\mathcal{M}(\lambda_0)\Phi = \lambda_1\Phi$ for the eigenvalue λ_1 with the largest real part. Further iterates are computed from the recursion $\mathcal{M}(\lambda_i)\Phi = \lambda_{i+1}\Phi$. Numerically, we found that this iterative approach converged rather rapidly to a real-valued eigenvalue for both $q = 2$ and $q = 3$.

By varying the parameter K_q, our numerical approximation of the principal eigenvalue of (4.13) is plotted for $q = 2$ and $q = 3$ in Figure 10. The results shown in Figure 10 suggest that (4.13) has no unstable eigenvalues for any $K_q \geq 0$. As a result, we conclude that a single hotspot steady-state solution is linearly stable.
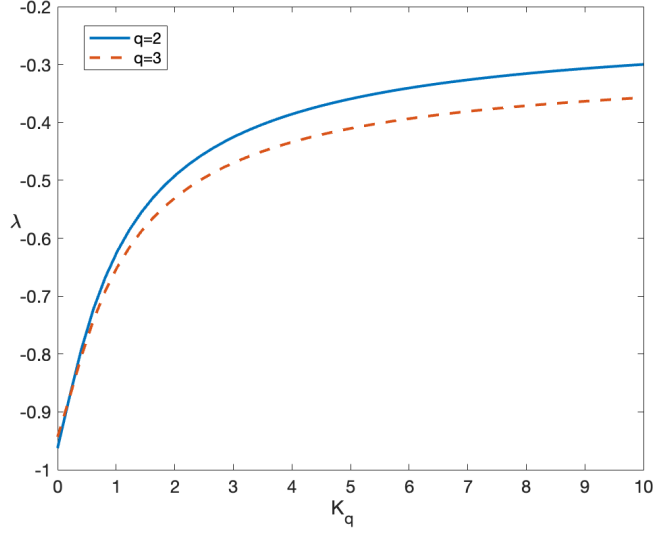
Figure 10: Numerical approximation of the principal eigenvalue of (4.13) for $q = 2$ and $q = 3$, with $K_q \in (0, 10)$. The parameter values are $\alpha = 1$, $\gamma = 2$, $\varepsilon = 0.02$ and $D = 5$. From (2.42) we obtain $V_0 = 0.0078$ for $q = 2$ and $V_0 = 0.0137$ for $q = 3$. We observe that λ is real, with $\lambda < 0$ for both $q = 2$ and $q = 3$.

4.3 Complex spatio-temporal dynamics of hotspot patterns

In this section, we compute the competition instability threshold D_c of the diffusivity D that triggers the collapse of a hotspot in a specific hotspot pattern. This occurs when an eigenvalue crosses above zero for the spectral problem (4.2) as the diffusivity D is increased. Threshold values for an oscillatory instability in the amplitudes of the hotspots are also computed numerically as τ is varied. These results for instability thresholds are then displayed in a phase diagram in the τ versus D parameter space. We remark that the vertical τ axis in this phase diagram determines the police diffusivity D_p via $D_p = D/\tau$. For a specific multi-hotspot pattern we will show that complex spatio-temporal hotspot dynamics can occur in a certain region of this parameter space.

Owing to the fact that the outer approximations for ψ and η in (4.2) satisfy spatially heterogeneous BVPs, it is rather intractable analytically to derive an NLEP for studying the linear stability of multi-hotspot equilibria. As such, we must proceed with a direct numerical approximation of the eigenvalue problem (4.2).

To approximate the discrete eigenvalues of (4.2), we first compute the steady-state A_e, V_e, u_e and their derivatives. To do so, for the full system (1.1) we use the finite difference method and discretize $A_e(x_j) \sim A_{ej}$, $\rho_e(x_j) \sim \rho_{ej}$, and $U_e(x_j) \sim U_{ej}$, where $x_j = j\Delta x$ for $j = 1, ..., N$ and $\Delta x = 2L/(N-1)$. In this way, we obtain N-dimensional steady-state vectors $\mathbf{A}_e \equiv (A_{e1}, \ldots, A_{eN})^T$, $\mathbf{V}_e \equiv \left(\rho_1/A_{e1}^2, \ldots, \rho_N/A_{eN}^2\right)^T$ and $\mathbf{u}_e \equiv \left(U_{e1}/A_{e1}^q, \ldots, U_{eN}/A_{eN}^q\right)^T$, as well as their derivatives $\mathbf{V}_{ex}$ and $\mathbf{u}_{ex}$ as approximated using central differences.

Next, we discretize (4.2) using finite differences. We discretize $\phi(x_j) \sim \phi_j$, $\psi(x_j) \sim \psi_j$, and $\eta(x_j) \sim \eta_j$, where $x_j = j\Delta x$ for $j = 1, ..., N$ and $\Delta x = 2L/(N-1)$. In this way, we obtain the matrix eigenvalue problem

$$\lambda \xi = A^{-1}(M + F)\xi, \tag{4.14}$$

where $\xi \equiv (\phi; \psi; \eta)^T$ is a $3N$ dimensional vector with $\phi \equiv (\phi_1, \ldots, \phi_N)^T$, $\psi \equiv (\psi_1, \ldots, \psi_N)^T$, and $\eta \equiv$

23

$(\eta_1, \ldots, \eta_N)^T$. The three block matrices A, M, and F in (4.14) are defined symbolically by

$$A \equiv \begin{pmatrix} \mathcal{I}_N & 0\mathcal{I}_N & 0\mathcal{I}_N \\ 2\mathbf{Diag}(A_e V_e) & \mathbf{Diag}(A_e^2) & 0\mathcal{I}_N \\ \tau q \mathbf{Diag}(A_e^{q-1} u_e) & 0\mathcal{I}_N & \tau \mathbf{Diag}(A_e^q) \end{pmatrix}, \qquad M \equiv \begin{pmatrix} \varepsilon^2 \mathbf{Lap} & 0\mathcal{I}_N & 0\mathcal{I}_N \\ M_{21} & M_{22} & 0\mathcal{I}_N \\ M_{31} & 0\mathcal{I}_N & M_{33} \end{pmatrix},$$

$$F \equiv \begin{pmatrix} \mathbf{Diag}(3A_e^2 V_e - 1) & \mathbf{Diag}(A_e^3) & 0\mathcal{I}_N \\ \mathbf{Diag}(-3A_e^2 V_e - (2+q)A_e^{1+q} u_e V_e) & \mathbf{Diag}(-A_e^3 - u_e A_e^{q+2}) & \mathbf{Diag}(-v_e A_e^{2+q}) \\ 0\mathcal{I}_N & 0\mathcal{I}_N & 0\mathcal{I}_N \end{pmatrix},$$

where $\mathcal{I}_N$ is the $N \times N$ identity matrix with the blocks of M defined by

$$M_{21} \equiv \mathbf{Diag}(2DA_{ex}V_{ex} + 2DA_e V_{exx}) + \mathbf{Diag}(2DA_e V_{ex})\mathbf{Der},$$
$$M_{22} \equiv \mathbf{Diag}(DA_e^2)\mathbf{Lap} + \mathbf{Diag}(2DA_e A_{ex})\mathbf{Der},$$
$$M_{31} \equiv \mathbf{Diag}(q(q-1)A_e^{q-2}A_{ex}u_{ex} + qA_e^{q-1}u_{exx}) + \mathbf{Diag}(qDA_e^{q-1}u_{ex})\mathbf{Der},$$
$$M_{33} \equiv \mathbf{Diag}(DA_e^q)\mathbf{Lap} + \mathbf{Diag}(qA_e^{q-1}A_{ex})\mathbf{Der}.$$

Here $\mathbf{Diag}(v)$ is defined as a square diagonal matrix with the elements of vector $\mathbf{v}$ on the main diagonal, while $\mathbf{Lap}$ and $\mathbf{Der}$ denote Laplacian and derivative operators.
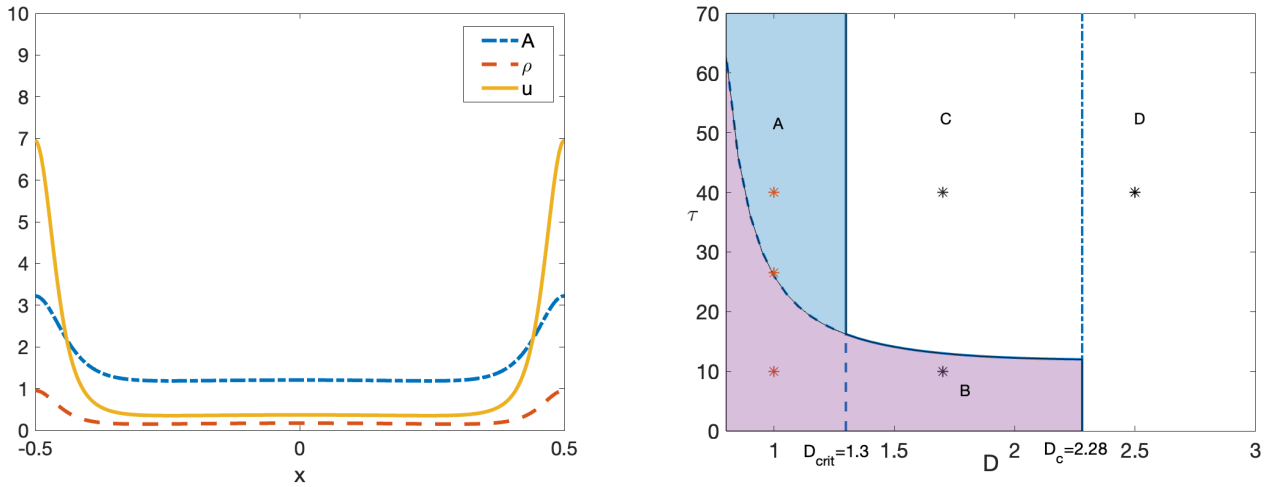

Figure 11: The two-boundary hotspot steady-state (left panel) and the linear stability phase diagram (right panel) for $L = 0.5$ with $\alpha = 1$, $\gamma = 2$, $q = 3$, $\varepsilon = 0.03$ and $U_0 = 1$. Left: steady-state for $D = 1.7$. Right: Linear stability phase diagram in the τ versus D plane computed from (4.14). The dot-dashed vertical line is the competition instability threshold D_c, which corresponds to a zero eigenvalue crossing, while the hyperbola-shaped curve is the Hopf bifurcation threshold. The solid vertical line is the hotspot nucleation critical value D_{crit} for a one-boundary hotspot steady-state. A two-boundary hotspot steady-state solution is unstable in the unshaded regions C, D and is linearly stable in the shaded region B. As τ is increased above a threshold in the region A, the two-boundary hotspot pattern exhibits nucleation-annihilation dynamics owing to the repeated effects of a near oscillatory collapse of a boundary hotspot that is prevented by a nucleation event occurring near the boundary. These two competing processes lead to large-scale and persistent hotspot amplitude oscillations.

For simplicity, and to eliminate the effect of slow hotspot dynamics, our numerical linear stability computations are restricted to a two-boundary hotspot steady-state solution, such as shown in the left panel of Figure 11.

24

As discussed below in §4.4, the results for this specific pattern will still apply to some other multi-hotspot steady-state patterns. To calculate zero-eigenvalue stability thresholds for this pattern, we use a bisection method to compute the critical value of D at which the real part of the principal eigenvalue of (4.14) crosses through zero. Hopf bifurcation thresholds are also computed for this pattern in a similar way. In the right panel of Figure 11, we plot the corresponding linear stability phase diagram for the two-boundary hotspot steady-states in the τ versus D parameter plane. In Figure 12, the path of the eigenvalues crossing from stable to unstable regions in the linear stability phase diagram are given at a few cross-sections of the phase diagram.

In the linear stability phase diagram of Figure 11, the dot-dashed vertical line is the competition instability threshold D_c at which the principal eigenvalue λ of the discrete approximation (4.14) crosses through zero. For $D > D_c$ (region D of Figure 11), the two-boundary hotspot steady-state is unstable owing to a positive real eigenvalue of (4.14) (see the middle row of Figure 12). This initial instability, termed a competition instability, has the effect of triggering a nonlinear event that monotonically annihilates one of the two boundary hotspots. In the unshaded region C of Figure 11, where $D < D_c$ and τ exceeds a threshold, the two-boundary hotspot steady-state is unstable as a result of a pair of complex conjugate eigenvalues that have entered into the right half-plane (see the top and bottom rows of Figure 12). If the emerging periodic solution branch is unstable, this instability is found numerically to trigger a nonlinear event leading to the oscillatory collapse of one of the two boundary hotspots, with the final pattern consisting of only one remaining boundary hotspot. This single-boundary hotspot is linearly stable and persists for all subsequent time. In Figure 13 we show the dynamics from full PDE simulations of (1.5) at the black marked points of Figure 11, which confirm the predictions from the linear stability phase diagram.

The solid vertical line in the right panel in Figure 11 is the hotspot nucleation threshold $D_{crit,\varepsilon}$, given in (2.26), for a single-boundary hotspot pattern. For $D < D_{crit,\varepsilon}$, there is no steady-state one-boundary hotspot solution and we predict that a nucleation event will occur that has the effect of creating a new boundary hotspot at the other endpoint of the domain. The dashed curve in the shaded region corresponds to the Hopf bifurcation threshold and it separates the shaded region in Figure 11 into two parts. In region B, corresponding to a sufficiently large police diffusivity, the principal eigenvalues of the linearization are complex conjugates that lie in the stable left-half plane. As such, an initial perturbation of the two-boundary hotspot steady-state solution will have asynchronous oscillations in the hotspot amplitudes that decay in time. In region A the two-boundary hotspot steady-state is unstable since the linearization has an unstable complex conjugate pair of eigenvalues.

To determine the linear stability of the time-periodic solution branch that emerges from this Hopf bifurcation across the boundary between regions A and B we use *pde2path* (cf. [29], [28]) on the PDE system (1.5) starting from the point $\tau_H = 25.94$ and $D = 1$ in the linear stability phase diagram of Figure 11. As we continue in τ, we observe from the left panel of Figure 14 that the periodic solution branch that emerges from the Hopf bifurcation is initially linearly stable. This indicates that the Hopf bifurcation is super-critical. The right panel in Figure 14 shows how the Floquet multipliers change along this periodic solution branch. To detect any secondary instability we computed 30 multipliers with the largest modulus as τ was varied, and a secondary instability was numerically identified with *pde2path* when at least one multiplier exceeded the tolerance $1 + \mathrm{fltol}$. In *pde2path*, the default value is $\mathrm{fltol} = 10^{-6}$ (see [28] for details on the algorithm in *pde2path* for calculating Floquet multipliers). The Floquet multiplier results in the right panel of Figure 11 show that the periodic solution branch loses stability at $\tau = 27.16$. Further numerical experiments (not shown) indicate that qualitatively similar results for the periodic solution branch occur on other vertical slices across regions A and B.

To verify this predicted behavior, in Figure 15 we show full PDE simulations of (1.5) at the three points marked in red in Figure 14 and the phase diagram of Figure 11. For $\tau = 10$ (see the left panel of Figure 15), the two-boundary hotspot steady-state is linearly stable to oscillations that decay as time increases. When τ slightly exceeds the Hopf bifurcation point, as seen in the middle panel of Figure 15, small persistent oscillations in the amplitudes of the two-boundary hotspots are observed. This is a signature of a linearly stable periodic solution that has emerged from a super-critical Hopf bifurcation. In contrast, for $\tau = 40$, which exceeds the threshold of the secondary instability along the periodic solution branch, in the right panel of Figure 15 we
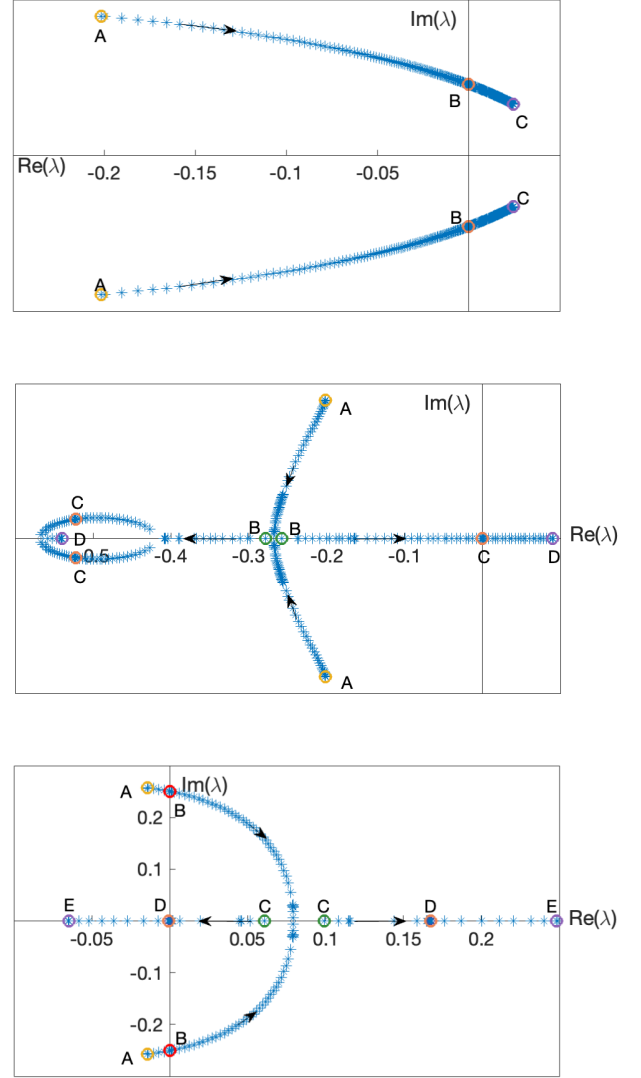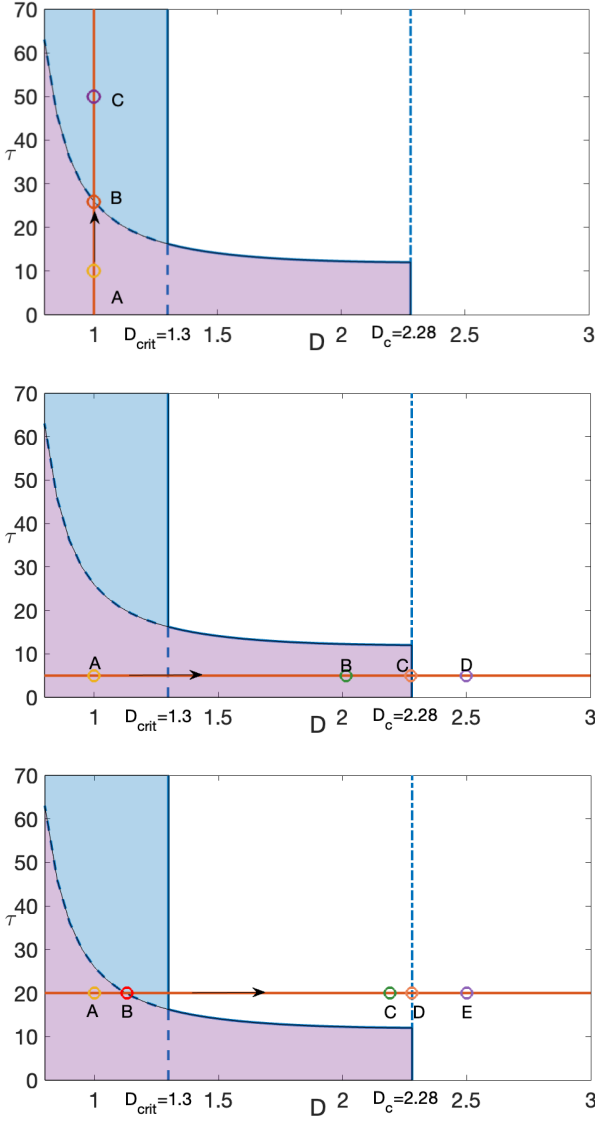
Figure 12: Plot of the numerically computed eigenvalues of (4.14) (right) along three cross-sections that cross from stable to unstable regions (left). Top row: As τ increases from 10 to 50 with $D = 1$, a pair of complex eigenvalues cross the imaginary axis at point B and indicates a Hopf bifurcation; Middle row: As D increases from 1 to 2.5 with fixed $\tau = 5$, a pair of complex eigenvalues transition to two real eigenvalues at point B. One of these eigenvalues crosses the origin on the real axis at point C and triggers an instability; Bottom row: As D increases from 1 to 2.5 with fixed $\tau = 25$, a pair of complex eigenvalues first cross the imaginary axis and enter the right-half plane at the Hopf bifurcation at point B. These eigenvalues merge onto the real axis at point C. As D increases further, one of these eigenvalues crosses the origin along the real axis, with the other eigenvalue remaining in the unstable right-half plane.

26

observe large-scale persistent asynchronous oscillations of the hotspot amplitudes. As distinct from the solution behavior in region C, for this value of $\tau = 40$ in region A, the resulting large-scale asynchronous oscillations in the hotspot amplitudes do not lead to an annihilation event in which only one hotspot remains. Instead, whenever a boundary hotspot has nearly been annihilated, a new hotspot will be nucleated at this boundary as there is no one-boundary hotspot steady-state solution. The overall effect of this *nucleation-annihilation* behavior is to provide large-scale persistent asynchronous oscillations in the hotspot amplitudes, where crime hotspots oscillate out of phase. Since regions A and C occur when τ is above a threshold, and when the criminal diffusivity D is below a threshold, we conclude that large-scale oscillations in the hotspot amplitudes will occur whenever the police diffusivity $D_p = D/\tau$ is too small.
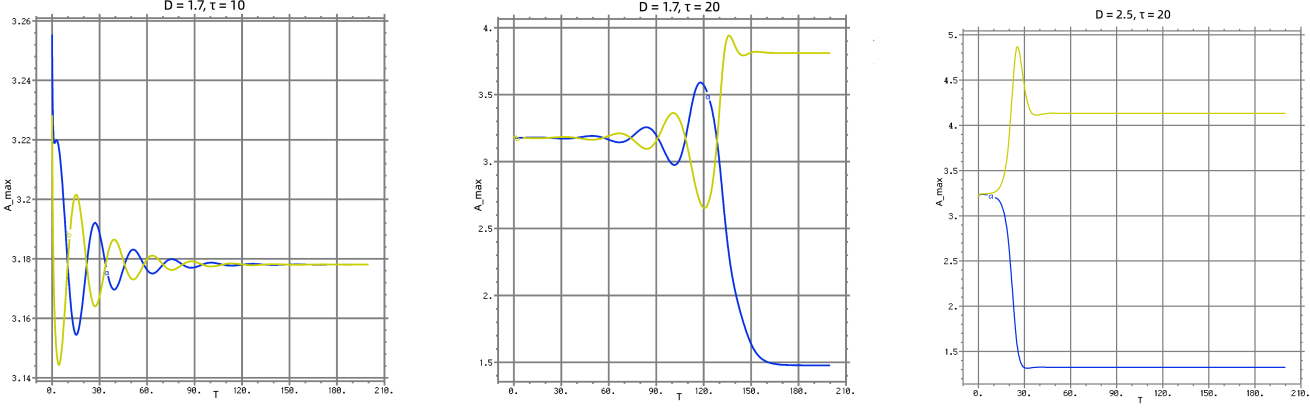

Figure 13: The hotspot amplitudes $A(\pm L)$ for a two-boundary hotspot pattern with D and τ as indicated at the black marked points in Figure 11. The left panel, for the point in region B of Figure 11, shows damped asynchronous oscillations in the hotspot amplitudes leading to a two-boundary hotspot steady-state. The middle panel, for the point in region C of Figure 11, shows an asynchronous oscillatory instability in the hotspot amplitudes that leads to the annihilation of one of the two boundary hotspots and a final one-boundary hotspot steady-state. The right panel, for the point in Region D of Figure 11, shows a competition instability that triggers hotspot annihilation. Parameters: $\alpha = 1$, $\gamma = 2$, $q = 3$, $\varepsilon = 0.03$, $L = 0.5$ and $U_0 = 1$.

4.4 Extension to some multi-spot steady-states

We now discuss how translation symmetry can be used to show that the phase diagram in the right panel of Figure 11 for the simple two-boundary hotspot pattern still provides some information as to where nucleation-annihilation dynamics can occur for some multi-hotspot patterns. This is illustrated in the left and right panels of Figure 16, where half and one-third of the pattern, respectively, replicates the two-boundary hotspot pattern in Figure 11. Here we note that one must increase U_0 to reflect the number of replications of the two-boundary hotspot pattern. For the multi-spot patterns in Figure 16, (3.25) still yields the nucleation threshold. Moreover, the numerical study of (4.14) determines both the competition instability threshold and the threshold for the initiation of the specific asynchronous mode of hotspot oscillations for which adjacent hotspots oscillate out of phase, which we refer to as the sign-alternating mode. For this particular type of asynchronous mode, the linear stability phase diagram in Figure 11 applies directly. We remark that for multi-hotspot patterns, there will likely be additional Hopf bifurcation thresholds for other possible modes of asynchronous oscillations other than the sign-alternating mode, which are not encapsulated in the phase diagram of Figure 11. For the $D = \mathcal{O}(\varepsilon^{-2})$ studied in [4], these additional Hopf thresholds were calculated for (1.1) for three and four-hotspot patterns.

However, for our prediction of nucleation-annihilation dynamics for multi-hotspot patterns it suffices to
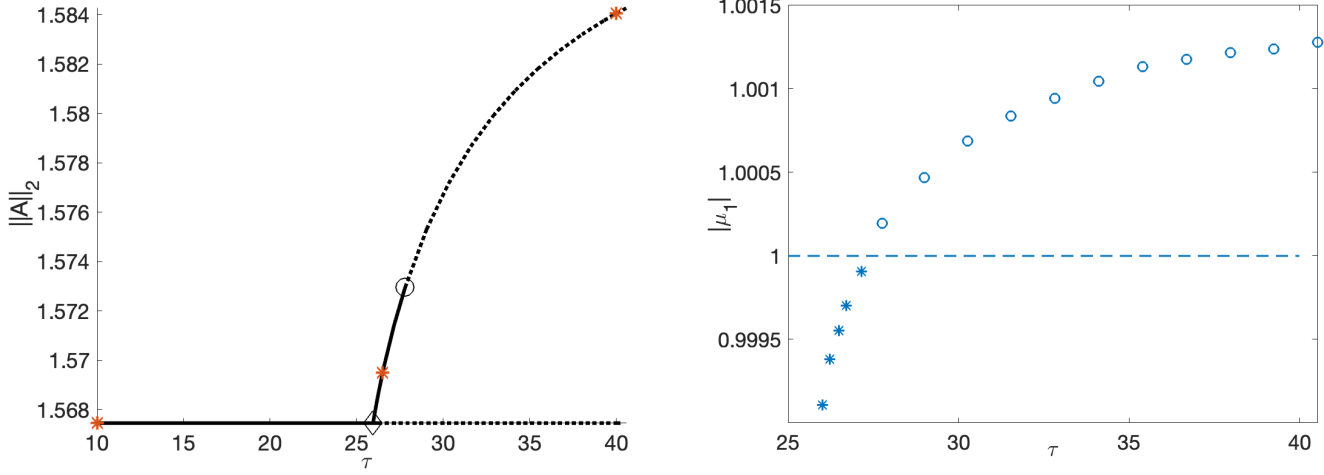
27

Figure 14: Left: The L_2-norm of A versus τ for steady-state and periodic solution branches as computed by *pde2path* for a vertical slice through the three red points in the phase diagram of Figure 11. A super-critical Hopf bifurcation of the steady-state occurs at $\tau_H \approx 25.94$. Right: Modulus of the Floquet multipliers computed by *pde2path* along the periodic orbit. The periodic solution branch loses stability at $\tau \approx 27.16$ as the Floquet multiplier μ_1 crosses the unit circle (i.e., $|\mu_1| > 1$). Parameters: $\alpha = 1$, $\gamma = 2$, $q = 3$, $\varepsilon = 0.03$, $L = 0.5$ and $U_0 = 1$.
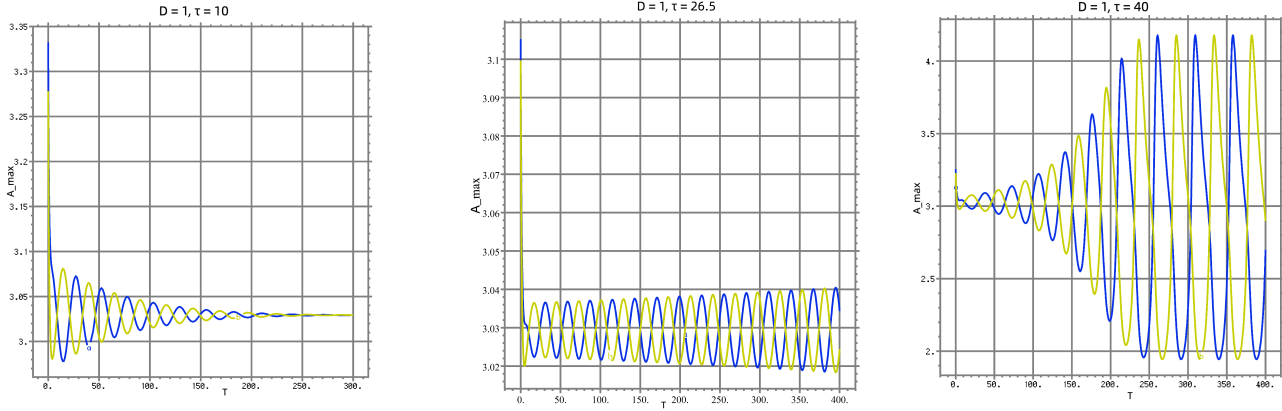
Figure 15: The hotspot amplitudes $A(\pm L)$ for a two-boundary hotspot pattern with $D = 1$ and τ as indicated at red marked points in Figure 11. Left: Damped asynchronous oscillations in the hotspot amplitudes lead to a two-boundary hotspot steady-state. Middle: Small persistent oscillations in the amplitudes of the two-boundary hotspots as τ slightly across the Hopf bifurcation point. Right: In Region A, and beyond the secondary bifurcation point on the periodic solution branch, large-scale persistent oscillations in the amplitudes of the two-boundary hotspots arise owing to the combined effect of an asynchronous oscillatory instability and hotspot nucleation behavior. Parameters: $\alpha = 1$, $\gamma = 2$, $q = 3$, $\varepsilon = 0.03$, $L = 0.5$ and $U_0 = 1$.

28

identify parameter values for which the sign-alternating mode has unstable hotspot oscillations and where hotspot nucleation will occur. In this way, region A of the phase diagram in Figure 11 can still be used to predict nucleation-annihilation dynamics for the specific patterns in Figure 16. As an illustration of this, in the movie in §1 accompanying Figure 4 (which corresponds to the right panel of Figure 16), nucleation-annihilation dynamics for (1.1) were found to occur at the indicated point in region A of the phase diagram in Figure 11.
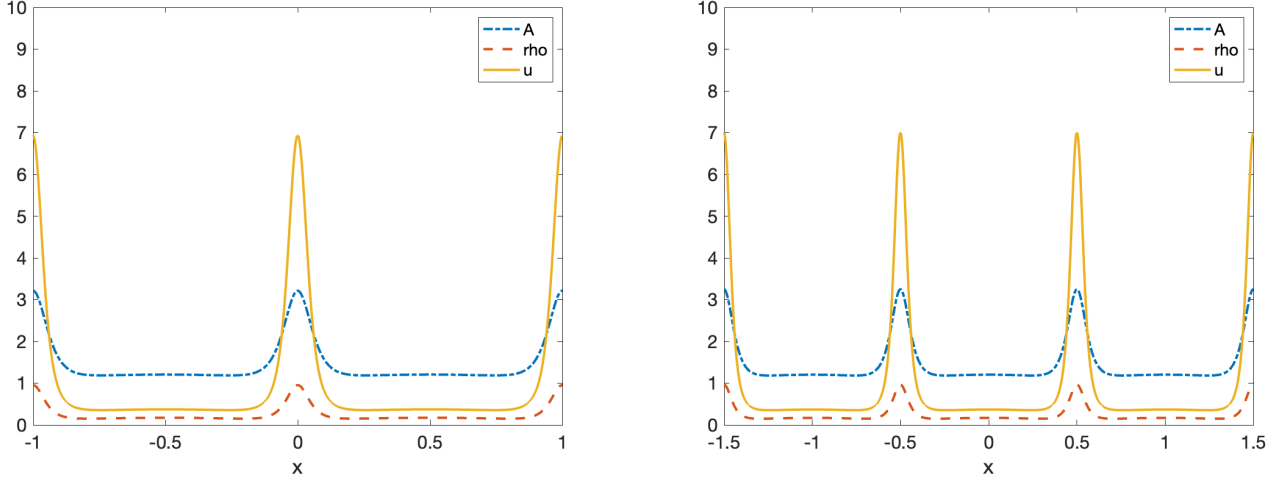
Figure 16: Two examples of steady-state multi-hotspot patterns with $D = 1.7$ where the linear stability phase diagram shown in Figure 11 applies. Parameters: $\alpha = 1$, $\gamma = 2$, $q = 3$, $\varepsilon = 0.03$. Here, $U_0 = 2$ and $L = 1$ for the left panel, with $U_0 = 3$ and $L = 1.5$ for the right panel.

5   Discussion

We have developed a hybrid asymptotic-numerical approach to study the existence and linear stability of steady-state hotspot patterns for the three-component RD model (1.1) of urban crime, which incorporates the effect of police deployment, in the new scaling regime where $D = \mathcal{O}(1)$. In this scaling regime, we have shown from a detailed study of a two-hotspot pattern that two opposing qualitative mechanisms can occur: one for hotspot nucleation and the other for hotspot annihilation. When these mechanisms are coincident in a parameter phase diagram we have predicted and verified from full PDE simulations that they lead to the occurrence of large-scale persistent spatio-temporal oscillations in the hotspot amplitudes for (1.1). Such complex spatio-temporal hotspot dynamics do not occur for the two-component crime model with no police intervention studied in [26], nor do they occur for the three-component model (1.1) in the scaling regime $D = \mathcal{O}(\varepsilon^{-2}) \gg 1$ studied in [4]. Moreover, we emphasize that they are intrinsic in certain parameter ranges for the deterministic system (1.1) when $D = \mathcal{O}(1)$ and are not due to any stochastic effects, such as those that are inherent in agent-based modeling [10]. As an interpretation of our findings, in the overlapping parameter regime where both hotspot annihilation and nucleation are coincident we suggest that the problem of predicting where and when hotspots will appear and then effectively disappear under the effect of a constant police deployment is rather intractable. Overall, our theoretical framework underlying the existence of nucleation-annihilation dynamics shares some similarities, but has a different mechanism, with the merging-emerging dynamics discovered in [16] and [9] for spike dynamics of a Keller-Segel chemotaxis model with logistic growth.

More specifically, in our analysis of (1.1) for the regime $D = \mathcal{O}(1)$, we have shown that the branch of one-hotspot steady-state solutions has a saddle-node bifurcation point in D below which there is no one-hotspot

29

steady-state. By using translation symmetry, the saddle-node point is readily identified for K-hotspot steady-states. Near this critical threshold in D, a normal form analysis together with bifurcation software was used to indicate why new hotspots will be nucleated from a quiescent background at the spatial midpoint between adjacent hotspots when D decreases below a threshold. This threshold depends on the total police deployment U_0 and the other parameters in (1.1), and we have provided a hybrid asymptotic-numerical approach to accurately predict this existence threshold even when ε is only moderately small. The asymptotic results have been confirmed with results from the bifurcation software *pde2path* [29, 18]. The accuracy of our prediction for this threshold relies heavily on the new exact solution in Lemma 1, which provides a highly accurate determination of the hotspot profile. This analysis extends, and improves, a related analysis in [26] for the two-component RD system with no police in the $D = \mathcal{O}(1)$ regime. One key mathematical challenge in extending the approach used in [26] for the two-component model to allow for police intervention was in developing an effective approach to deal with the spatially nonlocal reduced problem that arises from the three-component model. From the viewpoint of global bifurcation theory, the persistence of the saddle-node point even in the presence of police was the key feature responsible for hotspot nucleation events.

With regard to the linear stability of hotspot patterns, we derived an NLEP for a one-hotspot steady-state. From numerical computations of the spectrum of this NLEP we have shown that a one-hotspot steady-state is always linearly stable. This linear stability result for one-hotspot steady-states is qualitatively similar to that found in [26] in the absence of police, as well as in [4] for (1.1) in the regime $D = \mathcal{O}(\varepsilon^{-2})$. However, since it is analytically intractable to provide a similar NLEP analysis for multi-hotspot patterns, owing to the fact that the steady-state solution is spatially non-uniform between adjacent hotspots, a full numerical approach was used to obtain a phase diagram in the τ versus D plane that encapsulates the linear stability results. For the specific, but yet highly illustrative, two-boundary hotspot pattern our numerically-computed phase diagram showed that distinctly different solution behavior will occur in different ranges of τ and D. For large values of D, the hotspot steady-state is unstable to an initial competition instability that triggers a monotonic hotspot annihilation event, without any amplitude oscillations. In an intermediate range of D, and when the police diffusivity $D_p = D/\tau$ is too small, an asynchronous oscillatory instability in the hotspot amplitudes will occur owing to a secondary instability that arises on the periodic solution branch that emerges from a Hopf bifurcation. Our numerical evidence suggests that this asynchronous oscillatory instability will lead to the non-monotonic collapse of one of the two boundary hotspots. Moreover, for smaller values of D, we have shown that in the τ versus D phase diagram where the two-boundary hotspot steady-state is unstable to an asynchronous oscillatory instability in the hotspot amplitudes, but where a one-boundary hotspot solution does not exist, large-scale persistent spatio-temporal oscillations in the hotspot amplitudes will occur. In Figure 4 of §1 we showed that the phase diagram in the right panel of Figure 11 for the two-boundary hotspot pattern can also be used to predict a parameter set where nucleation-annihilation dynamics occur for some other multi-hotspot patterns (see also Figure 16).

Qualitatively extrapolating our linear stability and nucleation-threshold results to more complex spatial patterns than our simple two-boundary hotspot pattern, we conjecture that nucleation-annihilation dynamics, leading to large amplitude oscillations of hotspot amplitudes, will occur whenever τ and D are chosen so that an initial K-hotspot steady-state is unstable to an asynchronous oscillatory instability in the hotspot amplitudes, but where a steady-state pattern with fewer hotspots does not exist for that value of D. This should occur when the criminal diffusivity is below both the competition threshold and a saddle-node point, but for a sufficiently sluggish police deployment where the police diffusivity $D_p = D/\tau$ is also below a threshold. In such a parameter regime, whenever a hotspot is near collapse we predict that a new hotspot is effectively nucleated that prevents its annihilation. We conjecture that these competing processes lead to large-scale irregular oscillations in the hotspot amplitudes, whereby hotspots undergo repeated near-annihilation and nucleation events. Overall, such highly intricate dynamics for (1.1) provide a clear challenge for predicting when and where hotspots of crime will appear. In Figure 17 (see the movie in the Appendix) we show a full PDE simulation of (1.1) illustrating nucleation-annihilation dynamics for an initial pattern of two interior hotspots. From this figure, we observe that boundary hotspots are intermittently nucleated on the domain boundaries, while the interior hotspots undergo

repeated near oscillatory collapse and nucleation events. These irregular oscillations persist in time.
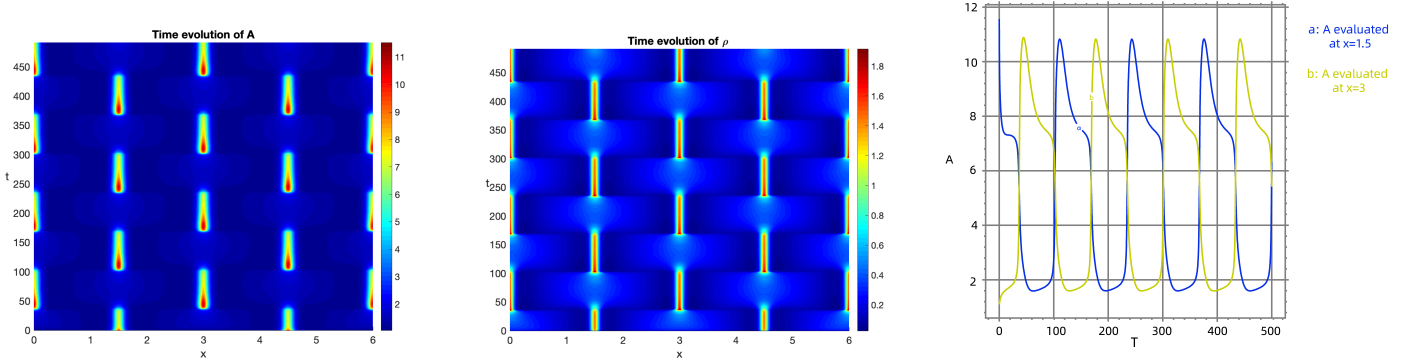

Figure 17: Nucleation-annihilation dynamics for an initial pattern with two interior hotspots. The left and middle panels are color plots of A and ρ, respectively, as time increases. The right panel is the amplitude of A versus time for the two interior hotspots centered at $x = 1.5$ and $x = 3$. Parameters: $\alpha = 1$, $\gamma = 2$, $q = 3$, $\varepsilon = 0.05$, $U_0 = 2$, $L = 3$, $D = 2.8$ and $\tau = 30$. (see Appendix C for the movie).

There are a few specific problems that warrant further investigation. Although our analysis of nucleation behavior still applies to multi-hotspot steady-state solutions, and the asymptotic results can be implemented for various ranges of parameters, the linear stability results and the phase diagram typically only apply to two-hotspot steady-states and the phase diagram must be recomputed as parameters are varied. As a result, it is rather challenging to identify the full range in the α, γ, τ, D, q, and U_0 parameter space where an initial two-hotspot steady-state pattern is expected to undergo complex spatio-temporal dynamics owing to the combined effect of hotspot nucleation and annihilation. In our proposed mechanism it is essential to numerically establish the existence of a secondary instability along the periodic solution branch that emerges from a Hopf bifurcation of the hotspot steady-state. In this context, it would be clearly worthwhile to numerically determine further phase diagrams in parameter space where complex spatio-temporal hotspot dynamics can occur.

An additional open direction would be to develop a weakly nonlinear analysis to derive a reduced model that fully characterizes nucleation-annihilation dynamics for (1.1). Such normal form reduced systems have been derived previously for certain three-component RD Fitzhugh-Nagumo type systems to theoretically model some highly intricate global dynamics of *weakly interacting pulses* that occur near co-dimension two bifurcation points (see [15] and the references therein). However, to date, there have been only a few weakly nonlinear theories developed for analyzing localized solutions for two-component RD systems in the *semi-strong pulse interaction* limit, in which only one species is localized ([30], [7], [11]). For semi-strong pulse interactions in the 1-D Gierer-Meinhardt model, a weakly nonlinear analysis has been used to show that spike amplitude oscillations arising from a Hopf bifurcation are subcritical ([30], [7]) and that competition instabilities leading to pulse annihilation are also subcritical [11]. For the highly nonlinear three-component system (1.1) with semi-strong interactions, it would be very challenging to develop weakly nonlinear theories near bifurcation thresholds.

Finally, it would be interesting to develop a similar hybrid approach to determine whether nucleation-annihilation dynamics are possible in a 2-D spatial domain. Two key challenges in a 2-D setting are that there is no explicit formula for the hotspot profile analogous to that in Lemma 1 and that the problem for approximating the hotspot nucleation threshold cannot be reduced to a quadrature as in the 1-D case.

A   Appendix A: The Homoclinic Profile

In this appendix we derive the explicit result in (2.7) of Lemma 1 for the profile of the homoclinic solution to (2.6), which satisfies $w_{yy} - (w - w_\infty) + (w^3 - w_\infty^3) = 0$. The first integral of this ODE yields

$$(w_y)^2 = -2\mathcal{F}(w), \qquad \text{where} \qquad \mathcal{F}(w) \equiv \int_{w_\infty}^w \left((s - w_\infty) - (s^3 - w_\infty^3)\right) ds. \tag{A.1}$$

By integrating $\mathcal{F}(w)$ and factoring the resulting expression, we obtain for $y < 0$, where $w_y > 0$, that

$$\sqrt{2}w_y = (w - w_\infty)(w_m - w)^{\frac{1}{2}}(w - w_{ms})^{\frac{1}{2}}. \tag{A.2}$$

We choose $y = 0$ to be where $w(y)$ has a maximum, and we label $w(0) = w_m$ where w_m is obtained from setting $\mathcal{F}(w_m) = 0$ in (A.1). In (A.2) we have

$$w_m \equiv -w_\infty + \sqrt{2 - 2w_\infty^2}, \quad w_{ms} \equiv -w_\infty - \sqrt{2 - 2w_\infty^2}, \quad w_m + w_{ms} = -2w_\infty, \quad w_m w_{ms} = 3w_\infty^2 - 2. \tag{A.3}$$

Here w_∞ is the smallest positive root of $w^3 - w + b = 0$, which satisfies $0 < w_\infty < 1/\sqrt{3}$ for any b in $0 \leq b < 2/(3\sqrt{3})$. As a result we have $w_{ms} < w_\infty < w_m$.

By separating variables in (A.2) we can write

$$\int \frac{dw}{(w - w_\infty)\sqrt{-(w + w_\infty)^2 + (2 - 2w_\infty^2)}} = \int \frac{1}{\sqrt{2}} dy. \tag{A.4}$$

We then introduce a new variable s defined by the positive root of

$$s^2 = -(w + w_\infty)^2 + (2 - 2w_\infty^2) \qquad \text{so that} \qquad w + w_\infty = \sqrt{2 - 2w_\infty^2 - s^2}, \tag{A.5}$$

on the range $w_\infty \leq w \leq w_m$. On this range of w, we observe that s is monotone decreasing, and that $s = \sqrt{2 - 6w_\infty^2}$ when $w = w_\infty$ and $s = 0$ when $w = w_m$. In terms of s, the left hand side of (A.4) can be written as

$$LHS = \int \frac{ds}{\left(\sqrt{2 - 2w_\infty^2 - s^2}\right)\left(2w_\infty - \sqrt{2 - 2w_\infty^2 - s^2}\right)} = \frac{1}{2w_\infty}(I_1 + I_2), \tag{A.6}$$

where $I_1 \equiv \int \frac{1}{\sqrt{2 - 2w_\infty^2 - s^2}} ds$ and $I_2 \equiv \int \frac{1}{2w_\infty - \sqrt{2 - 2w_\infty^2 - s^2}} ds$.

The integral I_1 is readily calculated as

$$I_1 = \sin^{-1}\left(\frac{s}{\sqrt{2 - 2w_\infty^2}}\right). \tag{A.7}$$

To calculate I_2, we multiply by the conjugate of the integrand to rewrite I_2 as

$$I_2 = -\int \frac{\sqrt{2 - 2w_\infty^2 - s^2} + 2w_\infty}{2 - s^2 - 6w_\infty^2} ds = I_{21} + I_{22}; \qquad I_{21} \equiv \int \frac{2w_\infty}{s^2 + 6w_\infty^2 - 2} ds, \quad I_{22} \equiv \int \frac{\sqrt{2 - 2w_\infty^2 - s^2}}{s^2 + 6w_\infty^2 - 2} ds. \tag{A.8}$$

By decomposing I_{21} into partial fractions, we calculate

$$I_{21} = -\frac{2w_\infty}{\sqrt{2 - 6w_\infty^2}}\tanh^{-1}\left(\frac{s}{\sqrt{2 - 6w_\infty^2}}\right). \tag{A.9}$$

32

To evaluate I_{22}, we use the following anti-derivative valid for $A > 0$ and $B > 0$:

$$\int \frac{\sqrt{A - x^2}}{x^2 - B^2}\, dx = -\frac{\sqrt{A - B^2}}{B}\tanh^{-1}\left(\frac{x\sqrt{A - B^2}}{B\sqrt{A - x^2}}\right) - \sin^{-1}\left(\frac{x}{\sqrt{A}}\right).$$

Identifying $A = 2 - 2w_\infty^2$, $B = \sqrt{2 - 6w_\infty^2}$, and $\sqrt{A - B^2} = 2w_\infty$ we determine I_{22} as

$$I_{22} = -\frac{2w_\infty}{\sqrt{2 - 6w_\infty^2}}\tanh^{-1}\left(\frac{s}{\sqrt{2 - 6w_\infty^2}}\frac{2w_\infty}{\sqrt{2 - 2w_\infty^2 - s^2}}\right) - \sin^{-1}\left(\frac{s}{\sqrt{2 - 2w_\infty^2}}\right). \tag{A.10}$$

Next, we substitute (A.9) and (A.10) into (A.8) to determine I_2. Upon using this expression for I_2, together with (A.7) for I_1, we obtain from (A.6) and (A.4) that

$$\tanh^{-1}\left(\frac{s}{\sqrt{2 - 6w_\infty^2}}\frac{2w_\infty}{\sqrt{2 - 2w_\infty^2 - s^2}}\right) + \tanh^{-1}\left(\frac{s}{\sqrt{2 - 6w_\infty^2}}\right) = -y\sqrt{1 - 3w_\infty^2}. \tag{A.11}$$

At the maximum value $w = w_m$ of the homoclinic, for which $s = 0$, (A.11) yields $y = 0$ as required. Then, by using the identity $2\tanh^{-1}(x) = -\ln(1 - x)/(1 + x)$ for $|x| < 1$, together with (A.5), we can exponentiate (A.11) to obtain on the range $0 \leq s \leq \sqrt{2 - 6w_\infty^2}$, for which $w_\infty \leq w \leq w_m$, that

$$\left(\frac{\sqrt{2 - 6w_\infty^2}(w + w_\infty) - 2w_\infty s}{\sqrt{2 - 6w_\infty^2}(w + w_\infty) + 2w_\infty s}\right)\left(\frac{\sqrt{2 - 6w_\infty^2} - s}{\sqrt{2 - 6w_\infty^2} + s}\right) = e^{2\kappa y}, \qquad \text{where} \qquad \kappa \equiv \sqrt{1 - 3w_\infty^2}. \tag{A.12}$$

Finally, we must eliminate s between (A.12) and (A.5) so as to determine $w = w(y)$. To do so, it is convenient to define η in $0 \leq \eta \leq 1$ by $s = \eta\sqrt{2 - 6w_\infty^2}$. From (A.12) and (A.5) we obtain the two equations

$$\left(\frac{\beta - \eta}{\beta + \eta}\right)\left(\frac{1 - \eta}{1 + \eta}\right) = e^{2\kappa y}, \qquad \eta^2(2 - 6w_\infty^2) = -4w_\infty^2\beta^2 + 2(1 - w_\infty^2), \tag{A.13}$$

where we have defined $\beta \equiv (w + w_\infty)/(2w_\infty)$. The first equation in (A.13) can be written as the quadratic

$$\eta^2 + \beta = -\frac{\eta(\beta + 1)}{\tanh(\kappa y)}. \tag{A.14}$$

Upon solving the second equation in (A.13) for η^2, we substitute into (A.14) to determine η as

$$-\frac{\eta(\beta + 1)}{\tanh(\kappa y)} = \frac{2(1 + \beta) - 2w_\infty^2(2\beta^2 + 3\beta + 1)}{2 - 6w_\infty^2} = \frac{(1 + \beta)}{2 - 6w_\infty^2}\left(2 - 2w_\infty^2(2\beta + 1)\right).$$

After cancelling the common factor $(\beta + 1)$, we obtain $\eta = -\tanh(\kappa y)\left(2 - 2w_\infty^2 - 4w_\infty^2\beta\right)/\left(2 - 6w_\infty^2\right)$, which we use in the second equation of (A.13) to eliminate η. Upon recalling that $\beta \equiv (w + w_\infty)/(2w_\infty)$, we get

$$\tanh^2(\kappa y)\left(2 - 2w_\infty^2 - 2w_\infty(w + w_\infty)\right)^2 = (2 - 6w_\infty^2)\left(-(w + w_\infty)^2 + 2 - 2w_\infty^2\right).$$

By using $\tanh^2(z) = 1 - \text{sech}^2(z)$, we obtain after some algebra that

$$\text{sech}^2(\kappa y)\left(2 - 2w_\infty^2 - 2w_\infty(w + w_\infty)\right)^2 = \left(2 - 2w_\infty^2 - 2w_\infty(w + w_\infty)\right)^2$$
$$+ (2 - 6w_\infty^2)\left((w + w_\infty)^2 - 2 + 2w_\infty^2\right), \tag{A.15a}$$
$$= (2 - 2w_\infty^2)\left((w + w_\infty) - 2w_\infty\right)^2. \tag{A.15b}$$

33

Finally, we define $c(y)$ by

$$c(y) = \sqrt{\frac{2}{1-w_\infty^2}}\,\text{sech}(\kappa y)\,, \qquad \text{where} \qquad \kappa \equiv \sqrt{1-3w_\infty^2}\,,$$

and we take the positive square root of (A.15b) to get

$$c\left(2 - 2w_\infty^2 - 2w_\infty(w+w_\infty)\right) = 2\left((w+w_\infty) - 2w_\infty\right).$$

By solving for $w+w_\infty$, we obtain the following result, which is equivalent to that given in (2.7) of Lemma 1:

$$w+w_\infty = \frac{c(1-w_\infty^2)+2w_\infty}{1+cw_\infty}\,,$$

B Appendix B: Calculation of the Integrals J_p

In this section, we compute the integrals $J_p \equiv \int_0^\infty (w^p - w_\infty^p)\,dy$, without having to use the explicit profile for $w = w(y)$. In our steady-state construction, leading to (2.42), we need to compute J_2, J_3, J_4, and J_5. Since (2.6) yields $w_{yy} - (w-w_\infty) + (w^3 - w_\infty^3) = 0$ we identify by integrating over $0 < y < \infty$ that $J_1 = J_3$. Moreover, since $y > 0$, we obtain that $w_y = -\left[-2\mathcal{F}(w)\right]^{1/2}$, where $\mathcal{F}(w)$ was given in (A.1).

B.1 Calculation of $J_1 = J_3$

We first write J_1 as

$$J_1 \equiv \int_0^\infty (w-w_\infty)\,dy = \int_{w_m}^{w_\infty}(w-w_\infty)\frac{dy}{dw}\,dw = -\int_{w_m}^{w_\infty}\frac{(w-w_\infty)}{\sqrt{-2\mathcal{F}(w)}}\,dw = -\sqrt{2}\int_{w_m}^{w_\infty}\frac{dw}{\sqrt{(w_m-w)(w-w_{ms})}}\,.$$

By introducing the new variable s by $w_m - w = s^2$, and using (A.3) to calculate $w_m - w_{ms}$, we get

$$J_1 = J_3 = 2\sqrt{2}\int_0^{\sqrt{w_m-w_\infty}}\frac{ds}{\sqrt{w_m - w_{ms} - s^2}} = 2\sqrt{2}\arcsin\left(\frac{\sqrt{w_m - w_\infty}}{2^{3/4}(1-w_\infty^2)^{1/4}}\right). \tag{B.1}$$

B.2 Calculation of J_2

To evaluate J_2, we proceed in a similar way to obtain

$$J_2 \equiv \int_0^\infty \left(w^2 - w_\infty^2\right)dy = -\int_{w_m}^{w_\infty}\frac{(w^2-w_\infty^2)}{\sqrt{-2\mathcal{F}(w)}}\,dw = -\sqrt{2}\int_{w_m}^{w_\infty}\frac{(w+w_\infty)}{\sqrt{(w_m-w)(w-w_{ms})}}\,dw\,.$$

Then, we introduce s by $w_m - w = s^2$ to obtain

$$J_2 = 2\sqrt{2}\int_0^{\sqrt{w_m-w_\infty}}\frac{w_m - w_{ms} - s^2}{\sqrt{w_m - w_{ms} - s^2}}\,ds + 2\sqrt{2}\int_0^{\sqrt{w_m-w_\infty}}\frac{w_{ms} + w_\infty}{\sqrt{w_m - w_{ms} - s^2}}\,ds\,.$$

This yields that

$$J_2 = 2\sqrt{2}\,(w_{ms} + w_\infty)\sin^{-1}\left(\frac{\sqrt{w_m - w_\infty}}{\sqrt{w_m - w_{ms}}}\right) + 2\sqrt{2}\int_0^{\sqrt{w_m-w_\infty}}\sqrt{w_m - w_{ms} - s^2}\,ds\,. \tag{B.2}$$

34

To evaluate the integral in (B.2), we use

$$\int_0^A \sqrt{B^2 - x^2}\, dx = \frac{B^2}{2} \sin^{-1}\left(\frac{A}{B}\right) + \frac{A\sqrt{B^2 - A^2}}{2}\,,$$

with $A = \sqrt{w_m - w_\infty}$ and $B = \sqrt{w_m - w_{ms}}$. Then, (B.2) becomes

$$J_2 = \sqrt{2}\,(w_{ms} + w_m + 2w_\infty)\sin^{-1}\left(\frac{\sqrt{w_m - w_\infty}}{\sqrt{w_m - w_{ms}}}\right) + \sqrt{2}\sqrt{-w_\infty^2 + w_\infty(w_m + w_{ms}) - w_m w_{ms}}\,.$$

677 Finally, we use (A.3) to notice that $w_{ms} + w_m + 2w_\infty = 0$ and to evaluate $w_m w_{ms}$. This yields the simple result

$$J_2 = \int_0^\infty \left(w^2 - w_\infty^2\right) dy = \sqrt{2}\sqrt{2 - 6w_\infty^2}\,. \tag{B.3}$$

678 **B.3   Calculation of J_4 and J_5**

The integral J_4 is calculated in a similar way as

$$J_4 \equiv \int_0^\infty (w^4 - w_\infty^4)\, dy = -\int_{w_m}^{w_\infty} \frac{(w^4 - w_\infty^4)}{\sqrt{-2F(w)}} dw = -\sqrt{2}\int_{w_m}^{w_\infty} \frac{(w^4 - w_\infty^4)/(w - w_\infty)}{\sqrt{(w_m - w)(w - w_{ms})}}\, dw$$

$$= -\sqrt{2}\int_{w_m}^{w_\infty} \frac{(w^2 + w_\infty^2)(w + w_\infty)}{\sqrt{(w_m - w)(w - w_{ms})}}\, dw\,. \tag{B.4}$$

Then, using the substitution $w_m - w = s^2$, the integral J_4 becomes

$$J_4 = 2\sqrt{2}\int_0^{\sqrt{w_m - w_\infty}} \frac{(w_m + w_\infty - s^2)\left((w_m - s^2)^2 + w_\infty^2\right)}{\sqrt{w_m - w_{ms} - s^2}}\, ds\,. \tag{B.5}$$

Similarly, we can rewrite $J_5 \equiv \int_0^\infty (w^5 - w_\infty^5)\, dy$, and by introducing the new variable $w_m - w = s^2$ we obtain
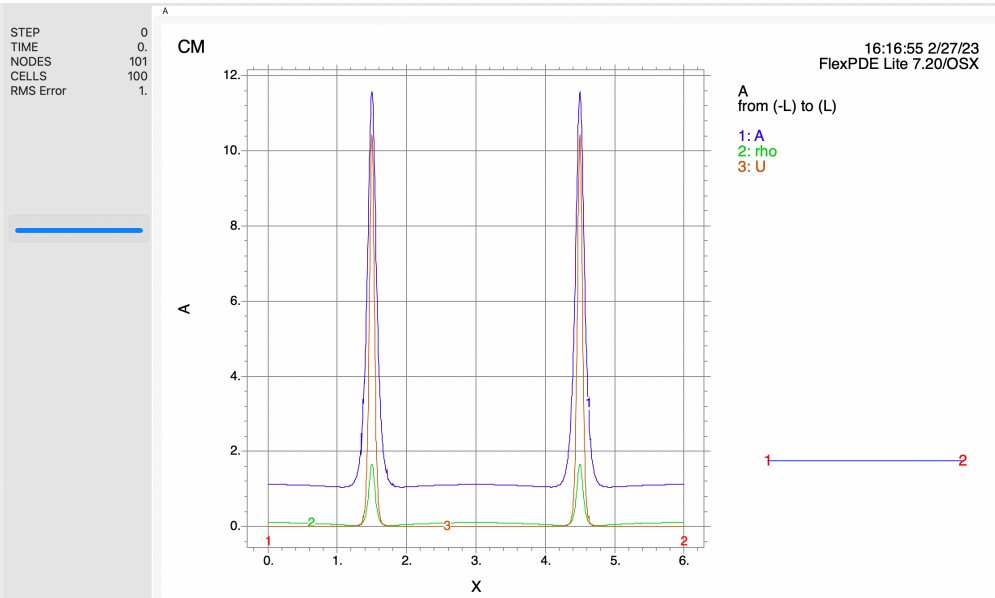
$$J_5 = 2\sqrt{2}\int_0^{\sqrt{w_m - w_\infty}} \frac{(w_m - s^2)^4 + w_\infty(w_m - s^2)^3 + w_\infty^2(w_m - s^2)^2 + w_\infty^3(w_m - s^2) + w_\infty^4}{\sqrt{w_m - w_{ms} - s^2}}\, ds\,. \tag{B.6}$$

679 The two integrals J_4 and J_5 are nonsingular and can be readily calculated numerically.
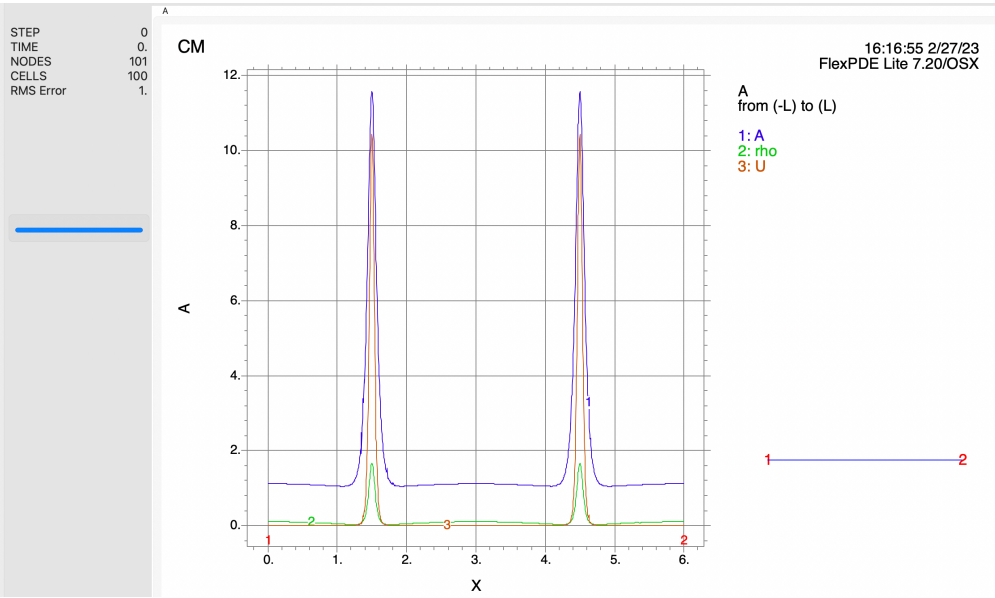
C   Appendix C: Illustration by Movies

C.1   Figure 2 (Left): Hotspot Nucleation.

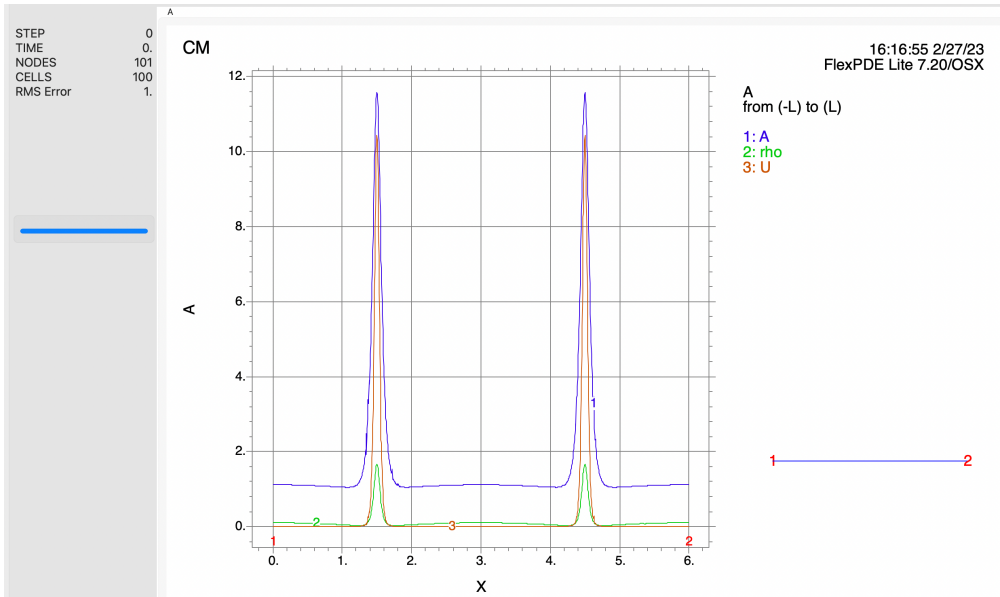## C.2   Figure 2 (Right): Hotspot Annihilation from a Competition Instability.

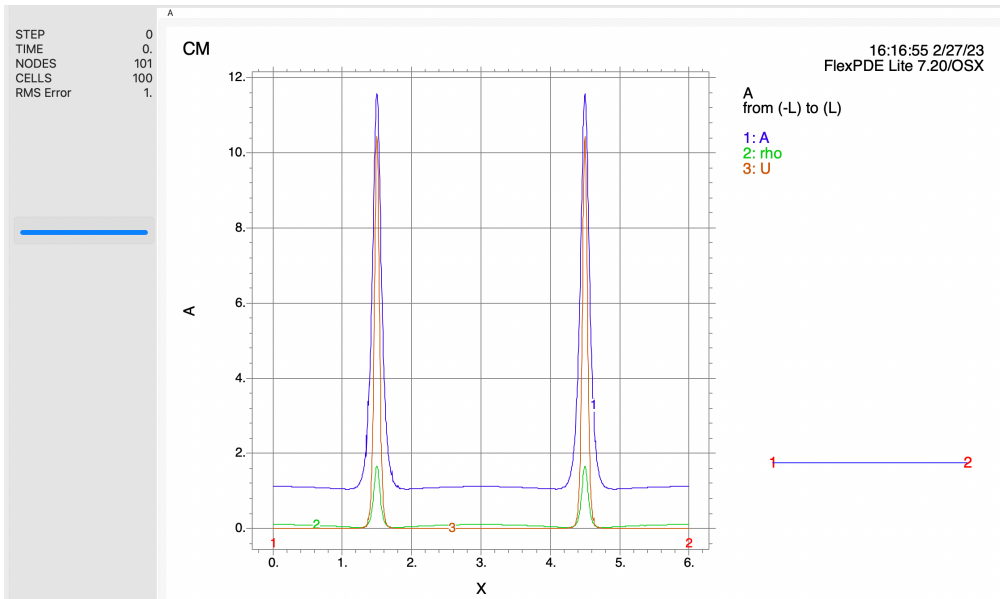## C.3   Figure 3: Asynchronous Amplitude Oscillations and an Oscillatory Collapse.

C.4   Figure 17: Complex Nucleation-Annihilation Dynamics.

Acknowledgements

References

[1] H. Berestycki, J. Wei, and M. Winter. Existence of symmetric and asymmetric spikes for a crime hotspot model. *SIAM J. Math. Anal.*, 46(1):691–719, 2014.

37

[2] A. A. Braga. The effects of hot spots policing on crime. *Ann. Am. Acad. Polit. S. S.*, 578:104–125, 2001.

[3] P. J. Brantingham and P. L. Brantingham. *Patterns in crime.* Macmillan New York, 1984.

[4] A. Buttenschoen, T. Kolokolnikov, M. J. Ward, and J. Wei. Cops-on-the-dots: The linear stability of crime hotspots for a 1-D reaction-diffusion model of urban crime. *European Journal of Applied Mathematics*, 31(5):871–917, 2020.

[5] A. Camacho, H. R. L. Lee, and L. Smith. Modeling policing strategies for departments with limited resources. *European Journal of Applied Mathematics*, 27(3):479–501, 2016.

[6] PDE FlexPDE. Solutions inc. *URL http://www. pdesolutions. com*, 2015.

[7] D. Gomez, L. Mei, and J. Wei. Hopf bifurcation from spike solutions for the weak coupling Gierer–Meinhardt system. *European Journal of Applied Mathematics*, 32(1):113–145, 2021.

[8] Y. Gu, Q. Wang, and G. Yi. Stationary patterns and their selection mechanism of urban crime models with heterogeneous near-repeat victimization effect. *European Journal of Applied Mathematics*, 28(1):141–178, 2017.

[9] T. Hillen, J. Zielinski, and K. Painter. Merging-emerging systems can describe spatio-temporal patterning in a chemotaxis model. *Discrete Contin. Dyn. Syst. Ser. B*, 18(10):2513, 2013.

[10] P. A. Jones, P. J. Brantingham, and L. B. Chayes. Statistical models of criminal behavior: the effects of law enforcement actions. *Mathematical Models and Methods in Applied Sciences*, 20(supp01):1397–1423, 2010.

[11] T. Kolokolnikov, F. Paquin-Lefebvre, and M. J. Ward. Competition instabilities of spike patterns for the 1-D Gierer-Meinhardt and Schnakenberg models are subcritical. *Nonlinearity*, 34(1):273–312, 2021.

[12] T. Kolokolnikov, M. J. Ward, and J Wei. Self-replication of mesa patterns in reaction–diffusion systems. *Physica D: Nonlinear Phenomena*, 236(2):104–122, 2007.

[13] T. Kolokolnikov, M. J. Ward, and J. Wei. The stability of steady-state hot-spot patterns for a reaction-diffusion model of urban crime. *Discrete & Continuous Dynamical Systems-B*, 19(5):1373–1410, 2014.

[14] D. J. B. Lloyd and H. O'Farrell. On localised hotspots of an urban crime model. *Physica D*, 253:23–39, 2013.

[15] Y. Nishiura, T. Teramoto, and K. I. Ueda. Arbitrarily weak head-on collision can induce annihilation: The role of hidden instabilities. *Japan Journal of Industrial and Applied Mathematics*, 40:1695–1743, 2023.

[16] K. Painter and T. Hillen. Spatio-temporal chaos in a chemotaxis model. *Physica D.*, 240(4-5):363–375, 2011.

[17] A. B. Pitcher. Adding police to a mathematical model of burglary. *European Journal of Applied Mathematics*, 21(4-5):401–419, 2010.

[18] J. Rademacher and H. Uecker. The OOPDE setting of pde2path—a tutorial via some Allen–Cahn models. 2018.

[19] N. Rodriguez. On the global well-posedness theory for a class of pde models for criminal activity. *Physica D*, 260:191–200, 2013.

[20] N. Rodriguez and A. L. Bertozzi. Local existence and uniqueness of solutions to a pde model for criminal behavior. *Mathematical Models and Methods in Applied Sciences (supp01)*, 20:1425–1457, 2010.

[21] N. Rodriguez, Q. Wang, and L. Zhang. Understanding the effects of on-and off-hotspot policing: Evidence of hotspot oscillating, and chaotic activities. *SIAM Journal on Applied Dynamical Systems*, 20(4):1882–1916, 2021.

[22] N. Rodriguez and M. Winkler. On the global existence and qualitative behavior of one-dimensional solutions to a model of urban crime. *European Journal of Applied Mathematics*, 33(5):919–959, 2022.

[23] M. B. Short, A. L. Bertozzi, and P. J. Brantingham. Nonlinear patterns in urban crime: Hotspots, bifurcations, and suppression. *SIAM Journal on Applied Dynamical Systems*, 9(2):462–483, 2010.

[24] M. B. Short, P. J. Brantingham, A. L. Bertozzi, and G. E. Tita. Dissipation and displacement of hotspots in reaction-diffusion models of crime. *Proceedings of the National Academy of Sciences*, 107(9):3961–3965, 2010.

[25] M. B. Short, M. R. D'Orsogna, V. B. Pasour, G. E. Tita, P. J. Brantingham, A. L. Bertozzi, and L. B. Chayes. A statistical model of criminal behavior. *Mathematical Models and Methods in Applied Sciences*, 18(supp01):1249–1267, 2008.

[26] W. H. Tse and M. J. Ward. Hotspot formation and dynamics for a continuum model of urban crime. *European Journal of Applied Mathematics*, 27(3):583–624, 2016.

[27] W. H. Tse and M. J. Ward. Asynchronous instabilities of crime hotspots for a 1-D reaction-diffusion model of urban crime with focused police patrol. *SIAM Journal on Applied Dynamical Systems*, 17(3):2018–2075, 2018.

[28] H. Uecker. Hopf bifurcation and time periodic orbits with pde2path – algorithms and applications. *Communications in Computational Physics*, 25(3):812–852, 2017.

[29] H. Uecker. *Numerical Continuation and Bifurcation in Nonlinear PDEs*. SIAM Publications, 2021.

[30] F. Veerman. Breathing pulses in singularly perturbed reaction-diffusion systems. *Nonlinearity*, 28(7):2211–2246, 2015.

[31] X. Zhao and J. Tang. Crime in urban areas: A data mining perspective. *ACM SIGKDD Explorations Newsletter*, 20(1):1–12, 2018.

[32] J. R. Zipkin, M. B. Short, and A. L. Bertozzi. Cops on the dots in a mathematical model of urban crime and police response. *Discrete & Continuous Dynamical Systems-B*, 19(5):1479, 2014.